Tectonothermal history of an exhumed thrust-sheet-top basin: An example from the south Pyrenean thrust belt

Pierre Labaume[1], Florian Meresse[1,2], Marc Jolivet[1,3], Antonio Teixell[4], and Abdeltif Lahfid[5]

[1]Laboratoire Géosciences Montpellier, Université de Montpellier, INSU-CNRS, Montpellier, France, [2]Now at Centre Scientifique et Technique Jean-Féger, Total, Pau, France, [3]Laboratoire Géosciences Rennes, Université de Rennes 1, INSU-CNRS, Rennes, France, [4]Departament de Geologia, Universitat Autònoma de Barcelona, Bellaterra, Spain, [5]BRGM, Orléans, France

Abstract This paper presents a new balanced structural cross section of the Jaca thrust-sheet-top basin of the southern Pyrenees combined with paleothermometry and apatite fission track (AFT) thermochronology data. The cross section, based on field data and interpretation of industrial seismic reflection profiles, allows refinement of previous interpretations of the south directed thrust system, involving the identification of new thrust faults, and of the kinematic relationships between basement and cover thrusts from the middle Eocene to the early Miocene. AFT analysis shows a southward decrease in the level of fission track resetting, from totally reset Paleozoic rocks and lower Eocene turbidites (indicative of heating to $T_{max} > \sim 120°C$), to partially reset middle Eocene turbidites and no/very weak resetting in the upper Eocene-lower Oligocene molasse ($T_{max} < \sim 60°C$). AFT results indicate a late Oligocene-early Miocene cooling event throughout the Axial Zone and Jaca Basin. Paleomaximum temperatures determined by vitrinite reflectance measurements and Raman spectroscopy of carbonaceous material reach up to ~240°C at the base of the turbidite succession. Inverse modeling of AFT and vitrinite reflectance data with the QTQt software for key samples show compatibility between vitrinite-derived T_{max} and the AFT reset level for most of the samples. However, they also suggest that the highest temperatures determined in the lowermost turbidites correspond to a thermal anomaly rather than burial heating, possibly due to fluid circulation during thrust activity. From these results, we propose a new sequential restoration of the south Pyrenean thrust system propagation and related basin evolution.

1. Introduction

The growth of orogenic fronts implies strong interactions between thrust displacement and propagation, vertical movements, and sediment transfer that contribute to maintaining the taper of the wedge [e.g., *Davis et al.*, 1983; *Dahlen*, 1990]. These interactions also determine burial/exhumation processes and hence the thermal evolution both in the orogenic belt and in its foreland basin. Quantifying these processes is thus crucial to understand the evolution of orogens, but this may be a difficult task when several detachment levels are involved in a complex wedge structure or when the thermal evolution is affected by fluid migration.

Given the exceptional preservation of synorogenic sedimentary sequences, the south Pyrenean basin is well suited for studying the relationships between thrusting and foreland and thrust-sheet-top basin evolution. However, certain aspects of the kinematic links between the basement thrusts forming the Axial Zone of the Pyrenees and the cover structures emerging in the basin remain debated due to insufficient knowledge of the deep structure of the basin and of the timing of the basement thrust sequence. These uncertainties also affect the understanding of the thermal history of the basin fill in terms of burial, exhumation, and fluid migration. Most of the previous medium- to low-temperature thermochronology studies ($^{40}Ar/^{39}Ar$, zircon and apatite fission tracks, and (U-Th)/He)) in the south Pyrenean thrust system concentrate on the Paleozoic basement rocks of the Axial Zone [*Morris et al.*, 1998; *Fitzgerald et al.*, 1999; *Sinclair et al.*, 2005; *Gibson et al.*, 2007; *Jolivet et al.*, 2007; *Maurel et al.*, 2008; *Metcalf et al.*, 2009; *Bosch et al.*, 2016]. Comparatively, few studies have been carried out in the Cenozoic south Pyrenean basin, with a limited number of samples which were mostly concentrated along the northern margin of the basin [*Beamud et al.*, 2010; *Filleaudeau et al.*, 2012; *Rahl et al.*, 2011; *Whitchurch et al.*, 2011; *Fillon et al.*, 2013; *Rushlow et al.*, 2013]. Furthermore, most of these studies are localized in the east central Pyrenees where, due to limited sediment burial, apatite fission tracks are generally weakly or not reset within the basin, and thus, they mostly reflect the exhumation history of the source areas rather than the thermal evolution of the basin fill.
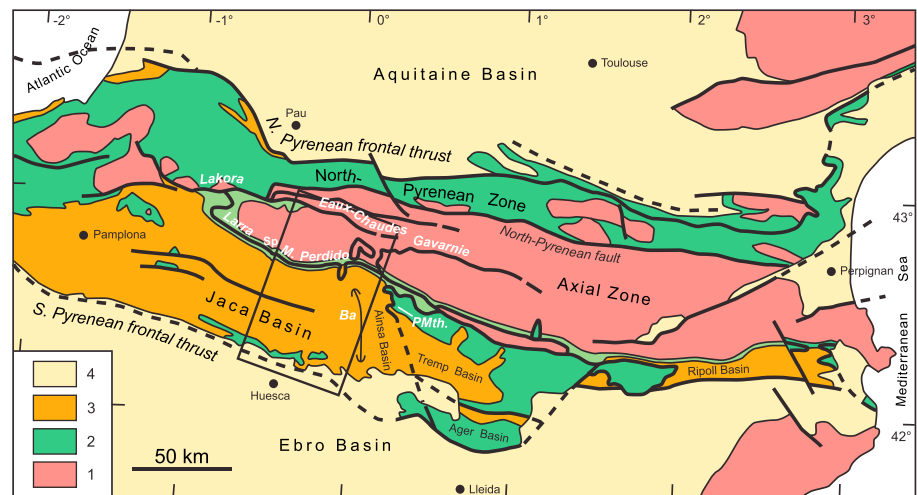
Figure 1. Structural sketch map of the Pyrenean orogen (simplified after *Teixell* [1996]). Box: study area (shown in Figure 2). Ba, Boltaña anticline; PMth, Peña Montañesa thrust; Sp, Somport pass; 1, Paleozoic rock units; 2, Mesozoic strata; 3, Cenozoic strata in thrust-sheet-top basins; and 4, Cenozoic strata in foreland (and Mediterranean) basins.

In this work, we combine detailed structural and thermochronological studies along a profile of the eastern Jaca thrust-sheet-top basin, from the southern part of the Axial Zone to the south Pyrenean thrust front. A cumulative thickness of up to 10 km of synorogenic sediments and a similar order of structural relief due to basement thrusting make this part of the southern Pyrenees suitable for analyzing the links between the activity of the Pyrenean thrust system and the kilometric scale vertical movements of burial and exhumation of the basin. Interpretation of industrial seismic reflection profiles provides the basis for the construction of a new balanced cross section constraining the geometry of the basement thrust system and its connections with the cover structures through the Triassic detachment level. The thermal history is investigated with apatite fission track analysis on 25 samples distributed along the whole section, including 18 samples in the basin fill providing the most complete thermochronological study to date across the south Pyrenean basin. Maximum paleotemperatures were also determined for some samples using vitrinite reflectance measurements and Raman spectroscopy of carbonaceous material. Inverse modeling of AFT and vitrinite reflectance data with the QTQt software [*Gallagher*, 2012] was made on key samples to test the compatibility between vitrinite-derived temperatures and AFT reset level. These data are integrated in a step-by-step restoration of the Jaca Basin deformation defining a new interpretation of the thrust propagation sequence, the distribution of shortening and displacement transfer, and the burial/exhumation history of foreland basin deposits that were incorporated in the thrust wedge as the Pyrenean orogen grew outward. We also show that the paleothermal record was affected by the occurrence of transient anomalies possibly related to hot fluid migration.

2. Geological Setting

2.1. The Pyrenean Belt

The Pyrenean belt is a doubly vergent collisional orogen formed from the Late Cretaceous to the early Miocene in relation to the northward subduction of the Iberian plate under the European plate [*Roure et al.*, 1989; *Muñoz*, 1992; *Vergés et al.*, 2002; *Teixell*, 1998; *Beaumont et al.*, 2000; *Mouthereau et al.*, 2014; *Teixell et al.*, 2016]. On the southern side of the belt, the south vergent thrust system (prowedge) comprises imbricated thrust units of Iberian Paleozoic basement which form the Axial Zone, connected to the south to detached thrust units of Mesozoic and Tertiary cover, which form the South Pyrenean Zone (Figure 1). The latter comprises synorogenic thrust-sheet-top basins of Paleogene age, partitioned in several subbasins by oblique thrust ramps splaying from a Triassic detachment level. To the south, the South Pyrenean Zone overrides the Ebro foreland basin. On the northern side of the belt, the North Pyrenean Zone (retro wedge) comprises a system of Mesozoic extensional basins inverted by the Pyrenean compression and thrust both southward above the Axial Zone and northward onto the Aquitaine foreland basin [*Roure et al.*, 1989;
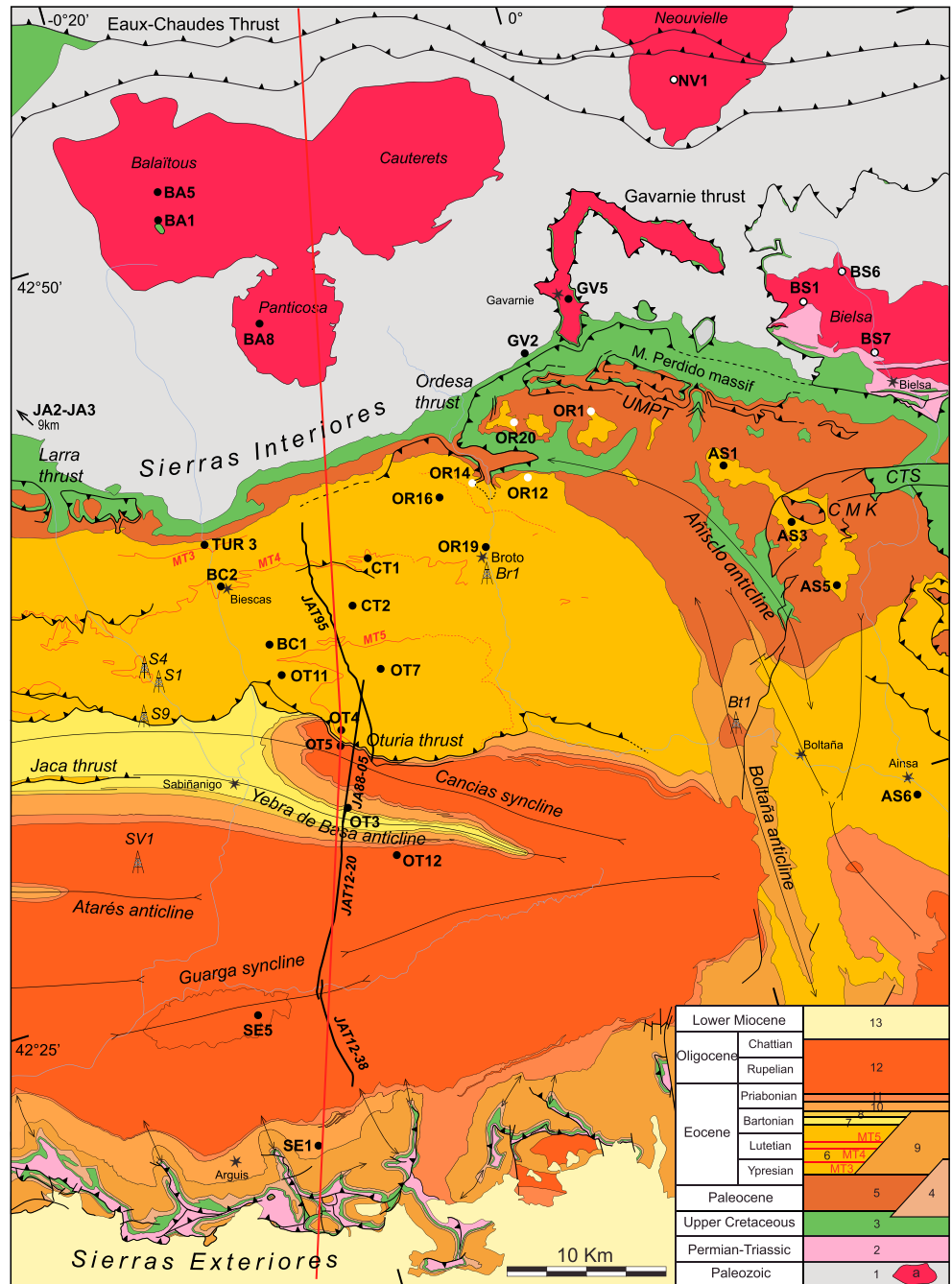
Figure 2. Detailed geological map of the study area in the eastern Jaca Basin (location in Figure 1). Data compiled from published maps [*Puigdefábregas Tomás*, 1975; *Gil Peña et al*., 1990; *Rios Aragües et al*., 1990; *Montes Santiago*, 1991; *Ternet et al*., 2003; *Millán Garrido*, 2006], completed with additional own field studies. Black dots: thermometry and apatite fission track samples (samples JA2 and JA3 are located west of the map in the Somport pass area, labeled Sp in Figure 1); white dots: nondatable samples, with thermometry results only; black circles in the Bielsa and Néouvielle granites: apatite fission track samples from *Jolivet et al*. [2007] cited in the text; black lines: seismic reflection profiles in Figure 6; derrick symbols: drill holes; red line: cross section in Figure 5. UMPT: Upper Monte Perdido thrusts; CMK: Castillo Mayor klippe; CTS: Cotiella thrust sheet. Inset legend: 1: pre-Permian (Hercynian) basement, including Hercynian granites (a; mostly migmatites in the Gavarnie window); 2: undifferentiated Permo-Triassic stratigraphic units (Bielsa massif) or Triassic Muchelkalk and Keuper (Sierras Exteriores); 3: platform carbonates and sandstones; 4: terrestrial red beds (Garumnian facies); 5: platform carbonates; 6: Hecho Group turbidites (MT3 to 5: carbonate breccia megabeds numbered according to *Labaume et al*. [1985]); 7: Larrés marl; 8: Sabiñánigo sandstone (delta); 9: Guara and Boltaña platform limestones; 10: Arguis-Pamplona marl; 11: Belsué-Atarés sandstone (deltaic); 12: Campodarbe Group (fluvial-alluvial); and 13: Uncastillo Formation (alluvial-fluvial).
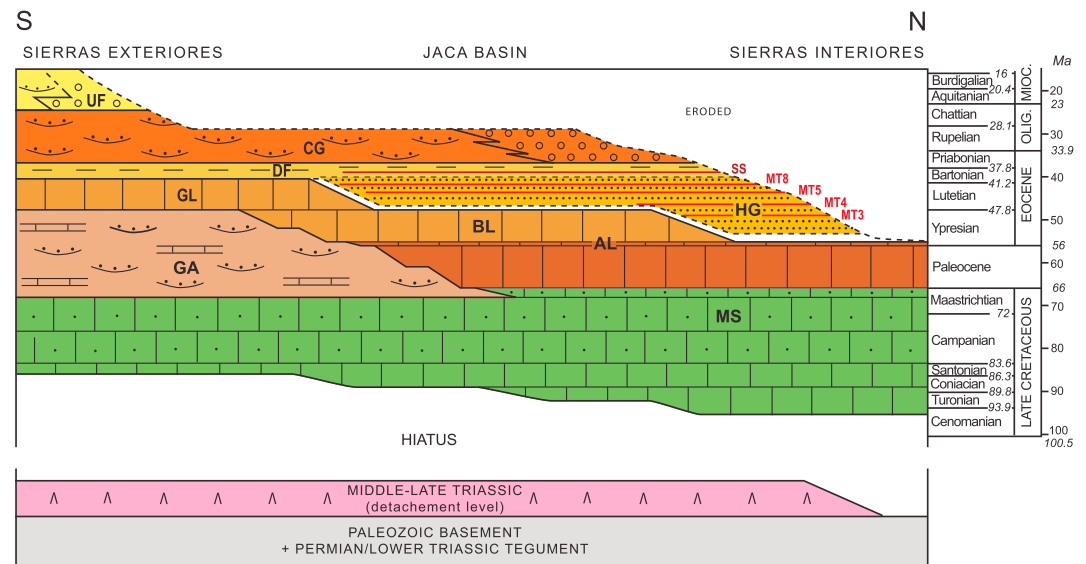
Figure 3. Chronostratigraphic diagram of the Jaca Basin fill along the north-south cross section shown in Figure 5 and localized in Figure 2 (red line). Time scale after *Cohen et al.* [2013]. AL: Alveolina limestone; BL: Boltaña limestone; GA: Garumnian terrestrial red beds; CG: Campodarbe Group (fluvial-alluvial); DF: deltaic facies (Larrés and Arguis-Pamplona marls and Belsué-Atarés sandstone); HG: Hecho Group turbidites; MS: Marboré sandstone; MT: carbonate breccia megabeds (numbered according to *Labaume et al.* [1985]); SS: Sabiñánigo sandstone (delta); UF: Uncastillo Formation (alluvial-fluvial).

Muñoz, 1992; *Vergés et al.*, 2002; *Teixell*, 1998; *Beaumont et al.*, 2000; *Mouthereau et al.*, 2014; *Teixell et al.*, 2016; *Jammes et al.*, 2009; *Lagabrielle et al.*, 2010].

Shortening across the belt remains debated. From balanced sections it has been estimated between 100 km [*Roure et al.*, 1989] and 165 km [*Beaumont et al.*, 2000] in the east central Pyrenees and to 80 km in the west central Pyrenees [*Teixell*, 1998]. The most recent estimations converge between 90 and 100 km of crustal shortening [*Mouthereau et al.*, 2014; *Teixell et al.*, 2016], mainly accommodated by the prowedge (south directed; ≥70% of the total shortening). To these values, there should be added the closure of a domain of exhumed mantle of uncertain width, most probably a few tens of kilometers [*Mouthereau et al.*, 2014; *Teixell et al.*, 2016].

2.2. The Study Area

The study area corresponds to a N-S transect across the eastern part of the south Pyrenean Jaca thrust-sheet-top basin and adjacent southern part of the Axial Zone (Figures 1 and 2). The Jaca Basin forms a vast E-W trending synclinorium characterized by Eocene and Oligocene synorogenic sediments located between the southern edge of Axial Zone (the Sierras Interiores in Figure 2) and the emerging south Pyrenean frontal thrust (the Sierras Exteriores in Figure 2). A few additional sampling localities are located in the NW part of the Ainsa Basin for comparison (Figure 2).

2.2.1. Lithostratigraphic Organization

The chronostratigraphic diagram in Figure 3 summarizes the general lithostratigraphic organization of the eastern Jaca Basin along a N-S profile, whereas Figure 4 shows a new synthesis of the stratigraphic ages based on a compilation of previous biostratigraphic and magnetostratigraphic studies correlated with a recent geomagnetic polarity time scale [*Gradstein et al.*, 2012].

The basement comprises Paleozoic rocks deformed during the Hercynian orogeny and intruded by late Hercynian granitoids, locally overlain by a tegument of post-Hercynian Permian-Lower Triassic detrital sediments [*Barnolas and Chiron*, 1996]. Middle-Upper Triassic shales, carbonates, and evaporites (Muschelkalk and Keuper facies) form the detachment level below most of the Jaca Basin (drilled in the Broto, Serrablo1 and San Vincente wells; Figure 2) and Sierras Exteriores; they disappear northward and are absent in the Axial Zone. The post-Triassic cover begins with Upper Cretaceous to lower Ypresian platform carbonates [e.g., *Puigdefàbregas and Souquet*, 1986]. The age of the basal transgression spans from the Cenomanian in
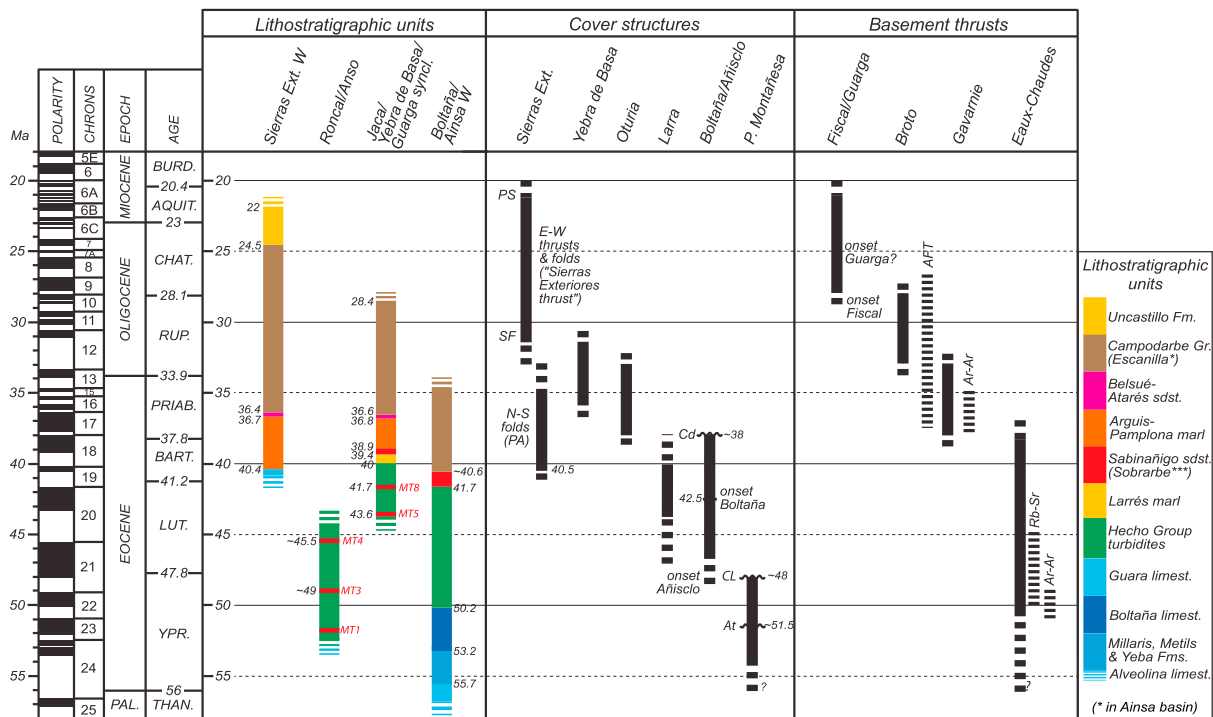
Figure 4. Table presenting a synthesis of the ages of stratigraphic units and timing of activity of the major tectonic structures of the Jaca Basin and adjacent Axial Zone. Stratigraphic ages are compiled from previous magnetostratigraphic and biostratigraphic studies with absolute ages of chrons and stratigraphic divisions corrected according to recent timescales [*Gradstein et al.*, 2012; *Cohen et al.*, 2013]. Timing of cover structures (deduced from growth strata and angular unconformities) are compiled from previous studies and additional own field observations. Timing of basement thrusts are based of geometrical features and displacement transfer considerations as discussed in the text. References for stratigraphic units: *Hogan and Burbank* [1996]; *Labaume et al.* [1985]; *Mochales et al.* [2012]; *Oliva-Urcia et al.* [2015]; *Oms et al.* [2003]. References for cover structures: *Hogan and Burbank* [1996], *Labaume et al.* [1985], *Poblet and Hardy* [1995], *Teixell* [1996], *Muñoz et al.* [2013], and *Oliva-Urcia et al.* [2015]. AFT: apatite fission track ages in the Néouvielle [*Jolivet et al.*, 2007] and Balaïtous (this work) granites; Ar-Ar: ^{40}Ar/^{39}Ar ages of K-feldspar in shear zones in the Néouvielle granite [*Jolivet et al.*, 2007] and authigenic illite from shear zones in the Gavarnie thrust fault zone [*Rahl et al.*, 2011]; At: Atiart unconformity; Cd: Campodarbe unconformity; CL: Charro-Lascorz unconformity; PA: Pico del Aguila anticline; PS: Peña del Sol thrust; Rb/Sr: Rb/Sr ages of shear zones in the Néouvielle granite [*Wayne and McCaig*, 1998]; and SF: San Felices thrust. The Peña Montañesa thrust sheet (cf. cover structures) is located in the Ainsa Basin (Figure 1) and is represented on the map in Figure 2 by the Castillo Mayor klippe (CMK in Figure 2).

the north to the Santonian in the south, and the carbonate succession thins southward, where its upper part shows a lateral change to terrestrial red beds.

In the northern part of the basin, the platform carbonates culminate with the lower Ypresian Alveolina limestone and are followed by the upper Ypresian to lower Bartonian turbidites of the Hecho Group, about 4000 m thick [e.g., *Mutti et al.*, 1988; *Remacha et al.*, 2003; *Oms et al.*, 2003; *Das Gupta and Pickering*, 2008; *Caja et al.*, 2009]. Much of the Hecho Group was fed axially from the east, but the uppermost turbidites show a northern provenance [*Remacha et al.*, 1987, 1998; *Roigé et al.*, 2016]. To the south, the turbidites onlap the coeval Boltaña and Guara platform limestones [*Labaume et al.*, 1985; *Puigdefàbregas and Souquet*, 1986; *Barnolas and Teixell*, 1994; *Mochales et al.*, 2012; *Muñoz et al.*, 2013]. Several (three in the study area) thick carbonate breccia megabeds derived from the southern shelf are intercalated in the siliciclastic turbidites of the Hecho Group [*Labaume et al.*, 1983, 1985, 1987; *Barnolas and Teixell*, 1994; *Payros et al.*, 1999].

From middle Bartonian to early Priabonian times, the turbiditic basin was progressively filled by westward prograding deltaic complexes (from bottom to top, the Larrés marl, the Sabiñánigo sandstone, the Arguis-Pamplona marl, and the Belsué-Atarés sandstone) [*Puigdefábregas Tomás*, 1975; *Remacha et al.*, 1987; *Hogan and Burbank*, 1996; *Dreyer et al.*, 1999]. Their accumulation was associated with a southward migration of the Jaca Basin depocenter with respect to the turbiditic stage, with a maximum thickness exceeding 2000 m in the central part of the basin [*Teixell*, 1996]. Above, the progradation of the terrestrial facies resulted in the deposition of the thick (~3500 m) Priabonian-Chattian Campodarbe Group, comprising east sourced fluvial deposits bordered to the north by north sourced alluvial fans [*Puigdefábregas Tomás*, 1975; *Montes Santiago*, 1992]. The Campodarbe Group is the youngest stratigraphic unit preserved in the Jaca Basin, where

its top is dated close to the Rupelian-Chattian transition [*Oliva-Urcia et al.*, 2015]. In the Ebro Basin, south of the thrust front, the top of the Campodarbe Group has been recently attributed to the late Chattian [*Oliva-Urcia et al.*, 2015] and is followed by the alluvial-fluvial Uncastillo Formation of late Chattian to early Burdigalian age [*Puigdefábregas Tomás*, 1975; *Arenas*, 1993; *Oliva-Urcia et al.*, 2015].

2.2.2. General Structure

2.2.2.1. Basement Thrusts

Previous works on the studied transect defined four main basement thrusts forming the south vergent Pyrenean thrust system. Two of them crop out in the Axial Zone: the Eaux-Chaudes thrust in the northern part and the Gavarnie thrust in the southern part (Figures 1 and 2). In the footwall of the Gavarnie thrust, two other basement thrusts have been inferred from the basement top culminations deduced from seismic reflection profiles and cross-section construction:

1. A basement thrust located below the northeastern Jaca Basin [*Cámara and Klimowitz*, 1985; *Mutti et al.*, 1988; *Teixell and Garcia-Sansegundo*, 1995], referred to as the Guara-Gèdre thrust by *Millán Garrido et al.* [2006]. An equivalent thrust, the Bielsa thrust, is inferred under the northern Ainsa Basin [*Cámara and Klimowitz*, 1985; *Casas et al.*, 2003; *Jolivet et al.*, 2007; *Fernández et al.*, 2012; *Muñoz et al.*, 2013].
2. The Guarga thrust, the southernmost basement thrust, is located under the central part of the Jaca and Ainsa basins [*Cámara and Klimowitz*, 1985; *Teixell and Garcia-Sansegundo*, 1995; *Teixell*, 1996; *Millán Garrido*, 2006; *Millán Garrido et al.*, 2006; *Fernández et al.*, 2012; *Muñoz et al.*, 2013].

2.2.2.2. Cover Thrusts

In the Sierras Interiores, the uppermost tectonic unit in the eastern Jaca Basin is the Monte Perdido thrust system, which comprises two detachment levels: (i) a lower detachment in the lowermost part of the Upper Cretaceous carbonates, which passes southward to a ramp cutting the whole Cretaceous-Tertiary carbonate succession in the Ordesa valley (the Ordesa thrust in Figure 2), and (ii) an upper system of smaller thrust units detached in the Campanian-Maastrichtian carbonates (UMPT in Figure 2) [*Séguret*, 1972; *Millán Garrido et al.*, 2006; *Fernández et al.*, 2012; *Muñoz et al.*, 2013]. Eastward, the Ordesa thrust and associated hanging wall anticline curve toward the southeast and pass laterally to the N-S Añisclo and Boltaña anticlines, which separate the Jaca Basin from the Ainsa Basin and are dated to the Lutetian-Bartonian by growth strata [*Soler-Sampere and Puigdefábregas-Tomás*, 1970; *Mutti et al.*, 1988; *Montes Santiago*, 1992; *Muñoz et al.*, 2013] (Figure 4).

In the central part of the Jaca Basin, the basin fill is cut by the Oturia thrust, which transported the Hecho Group turbidite succession over the deltaic complexes and the overlying alluvial conglomerates of the Campodarbe Group (Figure 2). In the thrust footwall, this succession is deformed by the ESE-WNW kilometric scale Cancias syncline and Yebra de Basa anticline, dated to the Priabonian-Rupelian by growth strata [*Puigdefábregas Tomás*, 1975; *Hogan and Burbank*, 1996] (Figure 4). The southern part of the Jaca Basin corresponds to the Guarga syncline which contains the Rupelian fluvial-alluvial deposits of the Campodarbe Group. At the southern edge of the basin, the structures linked to the emergence of the south Pyrenean frontal thrust consist of a complex association of E-W trending thrusts and folds (in the following globally referred to as the Sierras Exteriores thrust) superimposed onto older N-S detachment folds [e.g., *Puigdefábregas Tomás*, 1975; *Millán Garrido et al.*, 2000; *Millán Garrido*, 2006]. The N-S folds were dated from growth strata to the late Lutetian to early Rupelian by *Poblet and Hardy* [1995] and *Hogan and Burbank* [1996]. The recent magnetostratigraphic chart used here [*Gradstein et al.*, 2012] places the onset of N-S folding at 40.5 Ma (early Bartonian; Figure 4). Paleomagnetism studies showed that the N-S folds were initiated as NW-SE trending folds that progressively rotated clockwise during their growth [*Pueyo et al.*, 2002]. The Sierras Exteriores thrust was active from the middle Rupelian to early Miocene [*Hogan and Burbank*, 1996; *Teixell*, 1996; *Millán Garrido et al.*, 2000; *Millán Garrido*, 2006; *Oliva-Urcia et al.*, 2015] (Figure 4).

2.2.2.3. Basement-Cover Relationships

Due to the occurrence of a main detachment at the base of the cover succession [*Séguret*, 1972], the kinematic relationships between basement and cover thrusts in the southern Pyrenees are not straightforward and have been the subject of diverse interpretations. In the Jaca Basin, *Séguret* [1972] shows that the Monte Perdido thrust system is folded by, and therefore older than, the hanging wall culmination of the Gavarnie basement thrust. *Teixell* [1996] argues that the Monte Perdido thrust system is analogous to the Larra thrust, located in the western Sierras Interiores and deep rooted northward in the Lakora thrust [*Teixell*, 1990] (Figure 1). The later thrust branches laterally eastward with the Eaux-Chaudes basement thrust, suggesting that the Monte Perdido thrust roots within the latter [*Jolivet et al.*, 2007]. Due to the lateral
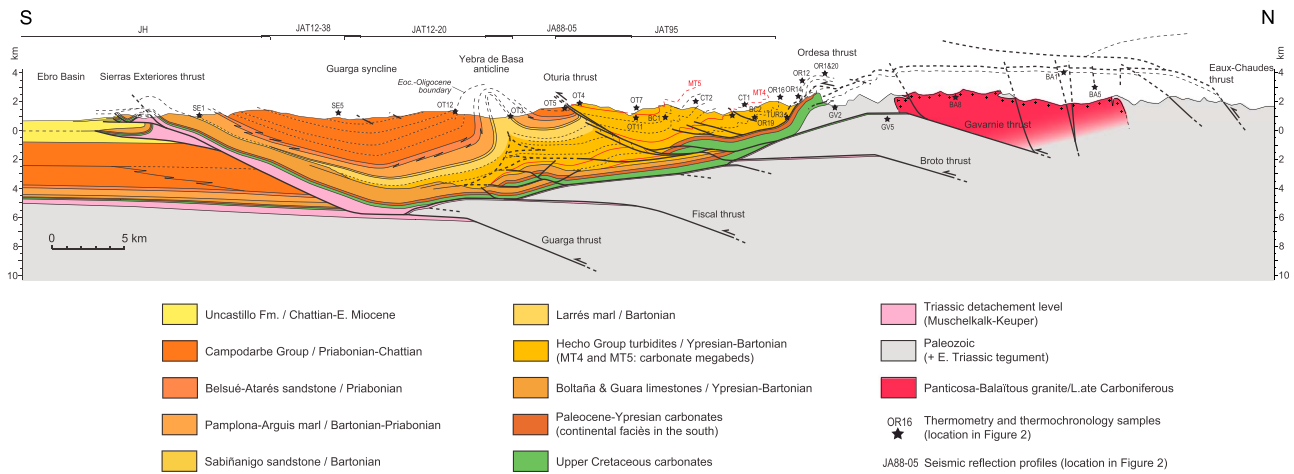
Figure 5. Balanced cross section of the eastern Jaca Basin (see Figure 2 for location). Surface data were compiled from published maps [*Puigdefábregas Tomás*, 1975; *Gil Peña et al.*, 1990; *Rios Aragües et al.*, 1990; *Montes Santiago*, 1991; *Ternet et al.*, 2003; *Millán Garrido*, 2006], complemented with own field observations. Subsurface structures are derived from the seismic interpretation shown in Figure 6. Seismic profiles and projected thermometry and apatite fission track samples are located in Figure 2.

continuity of the Ordesa thrust to the Boltaña anticline, *Mutti et al.* [1988] and *Teixell* [1996] assign a Lutetian-Bartonian age to the Monte Perdido and Larra thrust systems. *Teixell* [1996] relates the Priabonian-Rupelian thrust-fold structures of the central Jaca Basin (extending eastward in the Cancias-Yebra de Basa fold pair) to the Gavarnie thrust and the late Rupelian to early Miocene structures of the Sierras Exteriores to the Guarga thrust. More recently, *Millán Garrido et al.* [2006], followed by *Fernández et al.* [2012] and *Muñoz et al.* [2013], proposed that the Ordesa thrust is connected to the Gavarnie basement thrust and that only the upper units of the Monte Perdido thrust system are equivalent to the Larra thrust. Hence, *Huygue et al.* [2009], *Fernández et al.* [2012], and *Muñoz et al.* [2013] assign a Lutetian to Priabonian age to the Gavarnie thrust, and the two latter authors place the onset of the Guarga thrust activity in the early Rupelian. However, even if a connection between the Gavarnie and Ordesa thrust is geometrically possible below the Monte Perdido massif, this kinematic interpretation is inconsistent when following these structures to the west, where the Ordesa thrust is located (and tilted) above the Gavarnie thrust hanging wall culmination, reinforcing their kinematic distinction. Furthermore, west of the study area, *Labaume et al.* [1985] and *Teixell* [1996] show that the Larra thrust system, folded by, and hence older than, the Gavarnie basement thrust culmination, affects the whole Hecho Group turbidite succession and hence was active at least until the early Bartonian, coevally with the Boltaña anticline growth. These observations support the tectonic chronology proposed by *Teixell* [1996]; this issue is discussed further below in the light of the new cross section proposed in this paper.

3. Cross Section of the Eastern Jaca Basin

We present a new cross section of the eastern Jaca Basin (Figure 5; location in Figure 2), which illustrates the relationships between the major basement and cover thrust systems of this segment of the southern Pyrenees, and forms the basis for the interpretation of thermometry and thermochronology data distributed along the transect. The section was constructed on the basis of published geological maps [*Puigdefábregas Tomás*, 1975; *Gil Peña et al.*, 1990; *Rios Aragües et al.*, 1990; *Montes Santiago*, 1991; *Ternet et al.*, 2003; *Millán Garrido*, 2006], well logs (location in Figure 2) [*Instituto Geologico y Minero de España*, 1987], public industrial seismic profiles (available from the Instituto Geologico y Minero de España (IGME) website: <www.igme.es>), and own additional field observations. The seismic profiles selected for cross-section construction are located in Figure 2 and shown in Figure 6, but a number of other lines covering the domain shown in Figure 2 have also been analyzed. The identification of key stratigraphic horizons and depth conversion were based on well logs tied to seismic profiles and surface exposures.

3.1. Basement Thrusts

A refinement of the basement structure with the identification of five major basement thrusts has been achieved in this work (Figure 5). The first thrust is exposed within the Axial Zone, whereas the four others are subsurface.
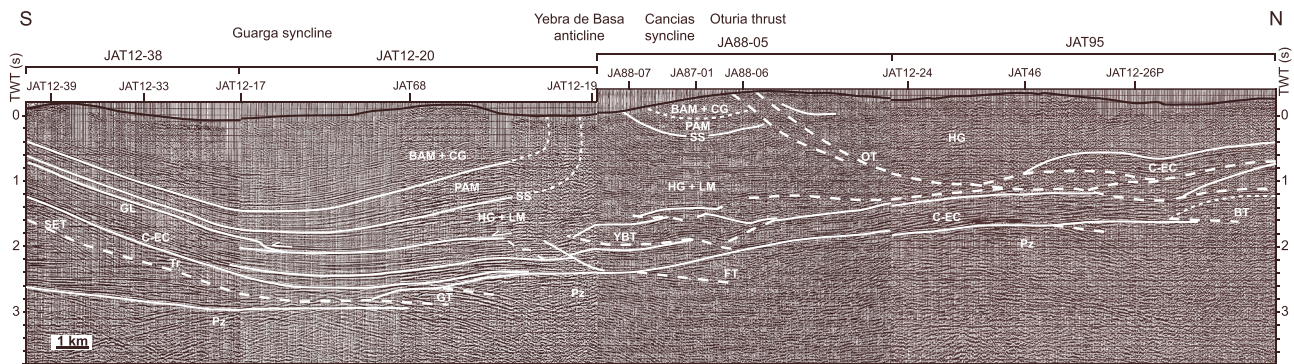
Figure 6. Interpretation of merged seismic reflection profiles JAT12-38, JAT12-20, JA88-05, and JAT95 from the eastern Jaca Basin (profiles available from the IGME website: <www.igme.es>). The line traces are shown in Figure 2 and follow approximately the cross section presented in Figure 5. Lithostratigraphic units: BAM + CG: Belsué-Atarés sandstone and Campodarbe Group; C-EC: Upper Cretaceous to lower Eocene carbonates; GL: Guara limestone; HG + LM: Hecho Group turbidites and Larrés marl; PAM: Arguis-Pamplona marl; PZ: Paleozoic; and SS: Sabiñánigo sandstone. Cover structures: OT: Oturia thrust; SET: Sierras Exteriores thrust; and YBT: Yebra de Basa thrust. Basement thrusts: BT: Broto thrust; FT: Fiscal thrust; GT: Guara thrust; and arrows: onlap of HG turbidites.

3.1.1. Eaux-Chaudes Thrust

To the north, the cross section intersects the Eaux-Chaudes thrust in basement rocks. In the thrust footwall, the top of basement (base of the Upper Cretaceous carbonates) is represented above the present-day topography by projecting outcrops located more to the west (Figure 2). In the hanging wall, we infer an eroded basement thrust unit, represented schematically with ~10 km displacement on the basis of the minimum displacement of 7 km observed more to the west in the Ossau valley [*Ternet et al.*, 2003].

3.1.2. Gavarnie Thrust

Immediately south of the Axial Zone, the syncline geometry of the sedimentary cover corresponds to the frontal limb of the Gavarnie thrust hanging wall culmination and allows locating the hanging wall cutoff of the basement. In the cross section, the elevation of the Gavarnie thrust is projected from the Gavarnie window (Figure 2) with a moderate westward plunge.

3.1.3. Broto, Fiscal, and Guarga Thrusts

In the Jaca Basin, seismic profiles feature a group of deep high-amplitude reflections, about 300 to 400 ms thick, which correspond to the Upper Cretaceous to Eocene carbonates (Figure 6). The base of this group of reflectors is used as a proxy for the top of the nonreflective Paleozoic basement, which shows a southward dip from the southern edge of the Axial Zone to the axis of the Guarga syncline, where it reaches a depth of approximately 6000 m below sea level. More to the south, the basement top displays a gentle northward dip corresponding to the foreland flexure. The inflection point corresponds to the leading edge of the basement thrust system, i.e., the Guarga thrust hanging wall cutoff [*Millán Garrido*, 2006; *Millán Garrido et al.*, 2006]. Steps in the imaged top of basement are interpreted as the hanging wall cutoffs of two other major thrusts, from north to south the Broto and Fiscal thrusts. The Broto thrust was already inferred in previous sections of the Jaca Basin (cf. above) while the Fiscal thrust has not been described before.

Displacement on the Gavarnie, Broto, Fiscal, and Guarga thrusts can be only indirectly estimated from the analysis of their hanging wall culminations according to the fault-bend fold model [*Suppe*, 1983], as was attempted by *Teixell* [1996] in the western Jaca Basin. Although a strict application of this model can be questioned because it may not adequately represent the deformation kinematics of the basement, it gives a basis for interpreting the fault-fold structure and determining plausible ranges of displacement values.

Projection of the Gavarnie thrust and its hanging wall culmination results in 8–10 km of thrust displacement, assuming a crestal-uplift stage of fault-bend folding for the structure. This value matches the minimum 7 km displacement observable in the Gavarnie window to the east and the 10 km inferred by *Teixell* [1996] more to the west. The Gavarnie thrust is folded by the crest of the Broto thrust hanging wall culmination, the geometry of which implies a displacement of 10.4 km on the later thrust. A flat top on the Fiscal thrust hanging wall culmination is not observed in seismic profiles close to the studied cross section, which, at first sight, could indicate a large hanging wall ramp with a minimum displacement of 13.2 km. However, we consider this value excessive as the seismic profiles show that the studied cross section is oblique to the trace of this thrust, oriented NW-SE in this area. A few kilometers to the east, the crest of the culmination is visible in

seismic profiles, allowing an estimation of displacement of 7–10 km for the Fiscal thrust. Finally, the geometry of the culmination of the Guarga thrust indicates a displacement of 4.8 km. These estimations are further discussed below (section 3.3).

3.2. Cover Thrusts

Four major cover thrusts are identified in the Jaca Basin along the studied cross section, which from north to south are the Ordesa, Oturia, Yebra de Basa, and Sierras Exteriores thrusts (Figure 5).

3.2.1. Ordesa Thrust

As discussed above, the Ordesa thrust corresponds to the sole thrust of the Monte Perdido thrust system, connected to the north to the Eaux-Chaudes basement thrust. The Ordesa thrust ramp across the carbonates is projected above the present-day topography from its exposure a few kilometers to the east (Figure 2). This ramp is here localized above the Gavarnie basement thrust culmination, and therefore, the two thrusts cannot be connected (cf. discussion above). To the south, the Hecho Group turbidites are affected by chevron folding at tens to hundreds of meter scale with axial plane regional cleavage [*Ten Haaf et al.*, 1970; *Séguret*, 1972; *Mutti et al.*, 1988; *Holl and Anastasio*, 1995; *Millán Garrido et al.*, 2006; *Izquierdo-Llavall et al.*, 2013]. In seismic profiles, these intensely folded turbidites are transparent whereas high-amplitude reflections corresponding to the underlying carbonates show a gentle folding (Figure 6). Accordingly, the chevron folding is interpreted as the frontal deformation of the Monte Perdido thrust system above a detachment located at the top of the carbonates.

The shortening by the Monte Perdido thrust system can hardly be determined in the study section, as most of the thrust unit is eroded. Shortening on the Ordesa thrust is probably around 1–2 km, based on its outcrop to the east (Figure 2). In the Monte Perdido massif, about 3 to 4 km of additional shortening occurs in the upper thrust units detached in the Campanian-Maastrichtian carbonates [e.g., *Trincal et al.*, 2014]. Hence, about 5 km of shortening can be inferred for the Monte Perdido thrust unit, but this is a minimum value as most of the unit is eroded above the Axial Zone. However, this value is consistent with that measured by *Teixell* [1996] on the equivalent Larra thrust at the western termination of the Axial Zone (Figure 1). As discussed above, the Ordesa thrust is dated as Lutetian-Bartonian from its lateral connection to the Añisclo and Boltaña anticlines.

3.2.2. Oturia Thrust

South of the zone of chevron folding, the turbidites dip gently northward in the hanging wall of the Oturia thrust. Seismic profiles show that the thrust dips moderately northward across the entire clastic succession, with the turbidites featuring a low-angle hanging wall ramp (Figure 6). Below the turbidites affected by chevron folding, seismic profiles show a thrust-fold structure in the carbonates, with a footwall ramp connected to the Triassic detachment level. The front of the structure is less well imaged and is interpreted as a duplex connected to the emerging Oturia thrust (Figure 5). In its footwall, the Oturia thrust cuts the northern limb of the Cancias syncline, which displays a fan geometry attesting folding during deposition since the Pamplona marl until the Santa Orosia conglomerate (lower Campodarbe Group), i.e., during most of the Priabonian. A few kilometers eastward, the Rupelian conglomerates (upper Campodarbe Group) do not show a fan geometry in the northern limb of the syncline. This structure suggests that the Oturia thrust derives from a Priabonian fault propagation fold cut by a late (late Priabonian-early Rupelian?) break-back thrust that propagated across the anticline hinge. Shortening on the Oturia thrust measured at the top of the carbonates is of 4.9 km.

3.2.3. Yebra de Basa Thrust-Fold Structure

The Cancias syncline is followed southward by the Yebra de Basa anticline. The steeply dipping limbs of the anticline are not clearly imaged in seismic profiles, while at depth there is a thrust-fold structure in the carbonates that we here define as the Yebra de Basa thrust (Figure 6). The tight geometry of the Yebra de Basa anticline observed at the surface implies a strong disharmony between the carbonates and overlying clastic succession, schematically represented as a multidetachment thrust system with fishtail thrust geometry, similar in style to other disharmonic thrust-fold systems [e.g., *Harrison*, 1995; *Dengfa and Suppe*, 2005]. We observed that the limbs of the Yebra de Basa anticline feature growth strata in the Campodarbe Group, attesting a late Priabonian-Rupelian age for the Yebra de Basa thrust-fold structure. However, erosion precludes observation of the end of folding. Shortening on the Yebra de Basa thrust measured at the top of the carbonates is 4.8 km.

Hence, the subsurface interpretation reveals connections of the Oturia thrust and Yebra de Basa anticline with deep thrust ramps across the carbonates. The westward lateral transition of the Yebra de Basa anticline

Table 1. Summary of Basement Thrust Ages and Kinematic Values

Basement Thrusts[a]	Age (Ma)[b]	Thrust Displacement (km)[b]	Total Shortening (km)[c]	Shortening Rate (mm/a)
Gavarnie	37.8–33.5	8	11	2.6
Broto	33.5–28	10.4	11.1	2
Fiscal	28–?	8.1	8.4	1.7[d]
Guarga	?–20	4.8	4.9	1.7[d]
TOTAL	38–20	31.3	35.4	2.0

[a]Thrusts are shown in Figure 5.
[b]Ages and displacements are discussed in the text.
[c]Sum of thrust displacement and hanging wall deformation.
[d]Calculated for Fiscal and Guarga thrusts as a whole.

to the Foz de Binies and Sierra de Illon thrust-fold structures involving the carbonate succession [*Labaume et al.*, 1985; *Teixell and Garcia-Sansegundo*, 1995] further supports this interpretation. This differs from the interpretation by *Millán Garrido et al.* [2006] who related these two structures to a detachment located at the top of the carbonates and connected to the Ordesa thrust.

3.2.4. Sierras Exteriores Thrust

Below the southern limb of the Guarga syncline, seismic profiles show the footwall ramp of the Sierras Exteriores thrust cutting across the whole succession and a detachment in the Keuper-Muschelkalk in the hanging wall [*Millán Garrido*, 2006; *Millán Garrido et al.*, 2000, 2006] (Figure 6). In the hanging wall succession, the lateral transition between the Guara limestone and the Hecho Group turbidites is visible on seismic profiles, with the turbidites onlapping erosional surfaces truncating the carbonates [*Barnolas and Teixell*, 1994] (Figure 6). The seismic profiles also image the wedge geometry of the whole Eocene succession, thickening northward and folded by the Guarga syncline. To the south, the leading edge of the Sierras Exteriores thrust sheet features a break-back thrust system cutting the cover succession up to the lower Miocene sediments of the Uncastillo Formation [*Millán Garrido*, 2006; *Millán Garrido et al.*, 2000, 2006]. The frontal unit, visible on seismic lines and cropping out 5 km to the east, is buried below the Uncastillo Formation, and its hanging wall ramp is eroded [*Millán Garrido*, 2006; *Millán Garrido et al.*, 2000, 2006]. Growth strata in the Uncastillo Formation date the break-back thrust sequence to the Chattian-early Miocene. However, the onset and end of Sierras Exteriores thrusting are difficult to determine on the cross section analyzed here and are discussed below. Shortening on the Sierras Exteriores thrust measured at the top of the carbonates is of 21.6 km, but this is a minimum value as the hanging wall ramp of the frontal unit is eroded.

3.3. Kinematic Relationships Between Cover and Basement Structures

The kinematic relationships discussed in this section are illustrated in the geochronological scheme of Figure 4 and summarized in Table 1 for the basement thrusts.

We have discussed above that the Eaux-Chaudes thrust comprises an eroded basement thrust sheet and a lower branch is connected to the Monte Perdido thrust system along a décollement above the Axial Zone, with speculative displacements around 10 km and 5 km, respectively. The Lutetian-Bartonian age of the Monte Perdido thrust system corresponds to the last stage of activity of the Eaux-Chaudes thrust. The onset of thrusting is more difficult to ascertain from available data. Absolute datings around 48–50 Ma by *Wayne and McCaig* [1998] and *Jolivet et al.* [2007] of shear zones cutting the Néouvielle granite and connected to the Eaux-Chaudes thrust (Figure 2) suggest that the latter was active from at least the early Eocene, before its propagation into the Jaca Basin (Figure 4).

The displacements on the Gavarnie, Broto, Fiscal, and Guarga basement thrusts are transferred to the cover through the Triassic décollement level. Deformation of the latter above the basement hanging wall culminations indicates a piggyback thrusting sequence for the four basement thrusts. However, determining precisely the kinematic relationships between the latter and the cover structures is not straightforward because they are separated by the décollement level. In the following, we attempt to balance displacements between the basement and cover structures for the different stages of deformation deduced from growth strata.

Seismic profiles show that the Oturia thrust can be connected only to the Gavarnie thrust (Figure 6), demonstrating for the latter a minimum displacement of 4.9 km during the Priabonian (-early Rupelian?). Hence, some displacement on the Gavarnie thrust must have been transferred south of the Oturia thrust to account

for the total of 8–10 km discussed above. However, the possibility that the 4.8 km displacement on the Yebra the Basa thrust is entirely related to the Gavarnie thrust is here discarded on the basis of the sequential restoration of the section, because it would imply insufficient elevation with respect to the basin and hence insufficient erosion of the Axial Zone during this period (see below, section 5). As a compromise, we propose (i) that the Gavarnie thrust was active during the Priabonian-earliest Rupelian with 8 km displacement, distributed in 4.9 km on the Oturia thrust during the whole period and 3.1 km on the Yebra de Basa thrust-fold from the late Priabonian, and (ii) that the 10.4 km displacement on the Broto thrust started in the earliest Rupelian and was partitioned into 1.7 km completing the Yebra de Basa thrust-fold and 8.7 km transferred to the Sierras Exteriores thrust. The onset of the Sierras Exteriores thrusting probably occurred during the early-middle Rupelian, similarly to the western Sierras Exteriores where it is dated to 31.3 Ma by the emplacement of the San Felices unit [*Hogan and Burbank*, 1996; *Millán Garrido et al.*, 2000; *Oliva-Urcia et al.*, 2015] (Figure 4). We note that the age here inferred for the Gavarnie thrust is consistent with the 36.5 Ma ^{40}Ar/^{39}Ar age of authigenic illite from the Gavarnie thrust fault zone [*Rahl et al.*, 2011]. The relays between the Broto, Fiscal and Guarga basement thrusts are difficult to determine with precision as the three thrusts are connected to the Sierras Exteriores thrust. The onset of the Fiscal thrust, uplifting the northern limb of the Guarga syncline, may have induced the end of the Campodarbe sedimentation in the Jaca Basin. The latter is not precisely dated as the preserved top of the succession (28.4 Ma according to *Oliva-Urcia et al.* [2015]) is an erosional surface, but we infer that the weathering-resistant San Juan de la Peña conglomerates present at the top of the Campodarbe Group are witnesses of the last sedimentation events. Hence, we assume that the onset of Fiscal thrusting may have occurred around 28 Ma. As the displacements on the Fiscal and Guarga thrusts (4.8 km for the latter) were transferred to the Sierras Exteriores thrust, the total shortening of 21.6 km calculated for the latter implies a displacement of 8.1 km for the Fiscal thrust, in agreement with the estimate discussed above. However, this is only a minimum value as the frontal unit of the Sierras Exteriores thrust system is eroded. This incertitude is discussed further below as it also has implications related to the N-S folding of the Sierras.

As the displacement on the Guarga thrust is smaller than on the Fiscal thrust, we assume that the relay between the two occurred during the late Chattian. We note that attributing the onset of the Guarga thrusting at the beginning of the Oligocene, as proposed by *Fernández et al.* [2012], implies that the Yebra de Basa thrust was connected to the Guarga thrust by a back directed detachment, a hypothesis for which there are no clues. Growth strata at the Sierras Exteriores show that the emergence of the Fiscal-Guarga thrusting continued until the early Miocene. More to the west, the youngest syntectonic sediments are dated around 22–23 Ma (Aquitanian) [*Hogan and Burbank*, 1996; *Arenas et al.*, 2001], but the youngest thrusts developed in a break-back sequence attest to a more recent age (up to early Burdigalian?) for the end of tectonic activity [*Millán Garrido et al.*, 2000]. In the following, we assume an end of the shortening around 20 Ma.

The shortening values (i.e., the sum of the fault displacement and hanging wall deformation) inferred from the cross section in Figure 5 for the Gavarnie, Broto, Fiscal, and Guarga basement thrusts are shown in Table 1. From these values, we derive an evolution of the shortening rates from 2.2 mm a^{-1} for the Gavarnie and Broto thrusts to 1.7 mm a^{-1} for the Fiscal and Guarga thrusts considered together. Although the accuracy of these calculations is limited by the uncertainties on the shortening values and thrusting ages, they suggest a progressive reduction of shortening rates across the wedge front. The rates here calculated are higher than those calculated by *Teixell* [1996] on the Ansó section for the equivalent structural domain (i.e., south of the Lakora thrust), but this is not surprising as the total shortening decreases from east to west in the south central Pyrenees.

3.3.1. The N-S Folds of the Sierras Exteriores

These folds do not appear in the study cross section which follows the axis of the Belsué syncline, close to the eastern limb of the Pico del Aguila anticline (Figure 2). The latter registered about 2.6 km shortening, dated by growth strata from the early Bartonian to early (middle) Priabonian [*Poblet and Hardy*, 1995; *Hogan and Burbank*, 1996] (Figure 4), and rotated clockwise about 40°during its growth [*Pueyo et al.*, 2002]. East of the Sierras Exteriores, the Boltaña anticline is reported to have rotated about 52° clockwise during Ypresian to middle Priabonian times, 40° of which from the late Lutetian and partially postfolding [*Mochales et al.*, 2012; *Muñoz et al.*, 2013]. Hence, the growth and rotation of the Sierras Exteriores N-S folds was contemporaneous of most of the Boltaña anticline rotation, during the last stage of the Eaux-Chaudes/Monte Perdido thrusting and part of Gavarnie thrusting. These kinematic relationships lead to interpret the Sierras Exteriores N-S folding as the result

of a westward propagation of deformation in the foreland of the Boltaña anticline [*Mochales et al.*, 2012], and hence, we do not relate it to the N-S shortening across the Jaca Basin, which propagated into the Sierras Exteriores frontal thrust ramp during the early-middle Rupelian (cf. above).

We infer that the rotation of the Sierras Exteriores folds may have implied the existence of a frontal E-W structure to separate the rotating domain from the fixed foreland. If it existed, this speculative structure is now eroded and the amount of contraction that it may have accommodated is unknown. Together with the erosion of the leading edge of the Sierras Exteriores thrust system, this contributes to the uncertainty on the N-S component of shortening on the Sierras Exteriores thrust.

4. Thermometry and Thermochronology

4.1. Methodology

Vitrinite reflectance measurements and Raman spectroscopy of carbonaceous material were used to determine the maximum paleo-temperatures that affected the Jaca Basin sediments along the studied section, while apatite fission track thermochronology allowed description of part of the exhumation history. Measurements were made on sandstone samples, coupling the three methods on the same sample wherever possible. The principles of the methods are described below. Technical details of analyses are given in the Appendix A.

4.1.1. Thermometry

4.1.1.1. Vitrinite Reflectance Measurements

Vitrinite is a vitreous organic material derived from the thermal evolution of botanic tissues mainly composed of lignin and cellulose [*Suárez-Ruiz et al.*, 2012]. The determination of vitrinite reflectance, measured under the microscope as the percentage of light reflected by a polished preparation in oil immersion, is a key method to estimate the level of thermal maturation of organic matter which evolved in the range of maximum paleotemperatures of 50–300°C. Here we report mean reflectance values (random reflectance, Rr%) measured under nonpolarized white light. Estimation of the maximum paleotemperature is made from the empirical correlation of vitrinite reflectance with independent thermal data (e.g., fluid inclusion data) compiled from basins all over the world. In this study, we used the calibration chart published by *Barker and Pawlewicz* [1994] for burial heating, with uncertainty of about ± 30°C.

4.1.1.2. Raman Spectroscopy of Carbonaceous Material (RSCM)

Raman spectroscopy is an analytical method that yields information on the molecular structure of the matter. It can be used to study the evolution of the structure of carbonaceous material (CM) and consequently to evaluate the maximum paleotemperature reached by rocks containing CM [*Beyssac et al.*, 2002; *Lahfid et al.*, 2010]. Spectra of perfect graphite are generally composed of one band situated at 1580 cm^{-1}. With the presence of disorder in the CM structure, additional bands, called defect bands, appear. In Raman spectra of very poorly ordered CM, at least four defect bands are observed [e.g., *Sadezky et al.*, 2005; *Lahfid et al.*, 2010], called the D1, D2, D3, and D4 bands and localized at 1350 cm^{-1}, 1620 cm^{-1}, 1500 cm^{-1}, and 1200 cm^{-1}, respectively. With the decrease of CM disorder, the defect bands disappear gradually, successively the D4, D3, and then D1 and D2 bands. A summary of the assignments of the different bands is given in *Sadezky et al.* [2005]. Here quantification of spectra evolution has been made using the RA1 parameter described in *Lahfid et al.* [2010], and that can be used to determine maximum paleotemperatures in the range 200–330°C (with uncertainty of ± 25°C) for rocks containing type II-III kerogen and buried under normal geothermal gradient. Temperatures lower than 200°C (with a lower limit at approximately 160°C) were estimated qualitatively comparing the obtained spectra to those of the Glarus area [*Lahfid et al.*, 2010].

4.1.2. Apatite Fission Track Thermochronology

Apatite fission track (AFT) thermochronology allows reconstruction of the thermal history of rocks through the temperature interval between ~120°C and ~60°C (the Partial Annealing Zone, PAZ) [e.g., *Fitzgerald et al.*, 1995; *Gallagher et al.*, 1998]. Over geological time scales, fission tracks in apatite anneal rapidly at temperatures higher than the PAZ whereas below 60°C, fission track annealing dramatically slows down to become nearly null. The limits of the PAZ may slightly vary since fission track annealing is partially controlled by the chemical composition of the apatite [*Donelick et al.*, 2005]. The D_{par} parameter (defined as the diameter of the etch pit measured on crystal sections parallel to the $<c>$ crystallographic axis) provides a relative estimate of the fission track annealing rate (varying with the chemical composition) in the individual
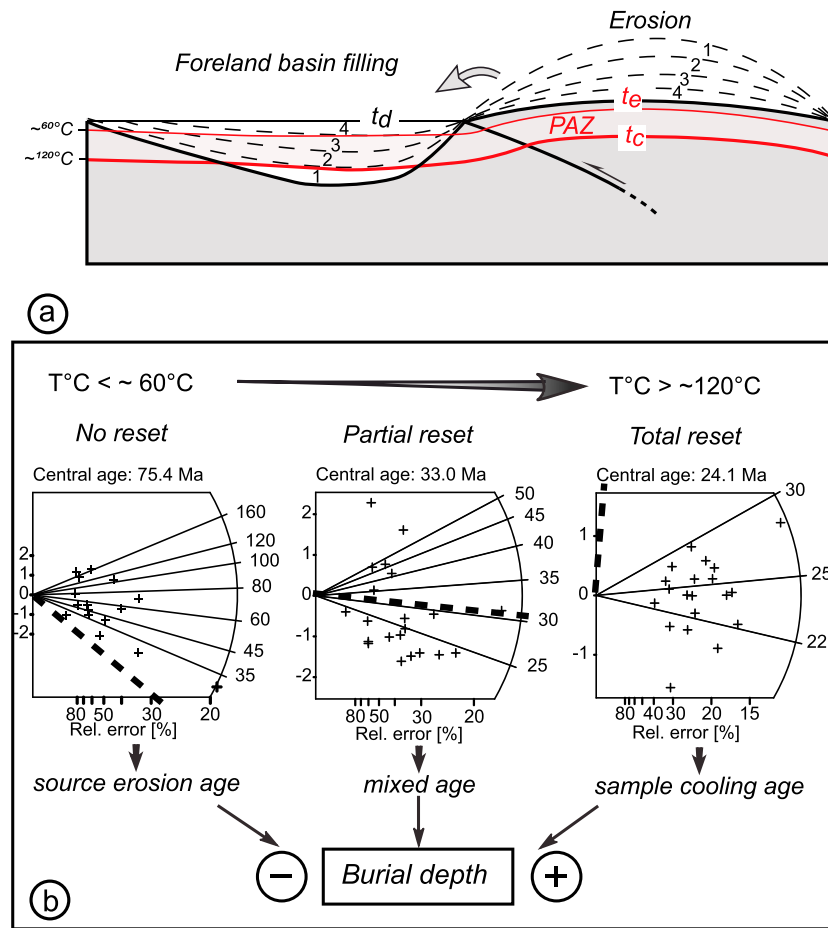
Figure 7. (a) Principles of apatite fission track thermochronology applied to a foreland basin setting (modified after *Braun et al.* [2006]). In the source area, rocks are progressively exhumed toward the surface, through the Partial Annealing Zone (PAZ), then eroded and deposited in the foreland basin. The cooling age (t_c) indicates the time at which the sample crossed the lower boundary of the PAZ. In the thickest part of the foreland basin, apatite grains from the layers 1, 2 and 3, and 4 are totally, partially, and not reset, respectively. The transport time being negligible, the depositional age (t_d) is equal to the age of exposure at the surface (t_e). (b) Significance of detrital apatite fission track ages. Variations in the apatite single-grain age are spread according to the reset level, plotted on radial diagrams [*Galbraith*, 1990], and compared to the depositional age of the sample (thick dashed line).

apatite crystals [*Donelick*, 1993, 1995; *Burtner et al.*, 1994; *Carlson et al.*, 1999; *Barbarand et al.*, 2003b; *Sobel and Seward*, 2010]. This allows estimation of the annealing properties for each sample and provides a sample/grain specific temperature range for track annealing [e.g., *Green et al.*, 1985; *Crowley et al.*, 1991; *Carlson et al.*, 1999; *Barbarand et al.*, 2003a; *Donelick et al.*, 2005]. In this study, D_{par} was measured on each analyzed grain.

Several samples showed evidence of overdispersion by failing the chi test ($P(\chi^2) < 10$) and having significant (>20%) age dispersion (Table 3). In order to fully describe these mixed ages, the single-grain age distribution was decomposed into statistically representative age populations or peaks ages using the BinomFit® software [*Brandon*, 2002]. Some other samples showing not negligible dispersion values (>5%), BinomFit® modeling was performed on all samples for methodological consistency. The main characteristic of the AFT ages being to decrease with the temperature increase [e.g., *Braun et al.*, 2006, Figure 3.8], statistical analyses allow us to qualitatively estimate for each sample the resetting level and therefore to follow the burial evolution of the data set.

In this study, the fission track age of each sample is expressed as the central age [*Galbraith and Laslett*, 1993] with ± 2σ uncertainties. Central ages seldom have a geological significance in terms of cooling age of the samples. In fact, detrital apatite age populations can correspond to three main scenarios (Figure 7):

Table 2. Paleothermometry Results

| | Vitrinite Reflectance | | | | | RSCM | | | |
| | | | | | | RA1 Parameter | | T (°C) | |
Sample[a]	Rr%	SD	MN	Q	T (°C)[b]	Mean	SD	Mean	SD
SE5	0.43	0,1	32	M	68				
OT3	0.35	0,04	30	I	<60				
OT5	0.62	0,06	15	M	97				
OT7	0.58	0.007	39	I	92				
OT4	0.60	0.09	26	M	95				
BC1	0.8	0.06	40	I	118				
CT2	0.64	0.08	37	M	100			<160	20
CT1	1.51	0.11	40	I	169			<160	20
BC2	1.28	0.10	40	I	156			<160	20
OR19	1.93	0.17	32	L	189			180	20
OR16	2.58	0.21	40	M	212			180	20
TUR3								180	20
OR14	3.79	0.28	50	M	244	0.56	0.012	236	10
OR12	2.98	0.21	50	I	224	0.56	0.005	238	6
OR20	3.92	0.28	51	M	247	0.57	0.012	238	13
OR1	4.54	0.26	50	M	259	0.59	0.011	270	10

[a]Samples are located on maps in Figures 2 and 8a, projected on cross sections in Figures 5 and 8b, and sample geographic coordinates are in Table 3; RSCM, Raman Spectroscopy of Carbonaceous Material; RA1 parameter, explanation in the text; Rr%, vitrinite mean reflectance (random reflectance); SD, standard deviation; MN, measurement number; Q, data quality (I, important; M, medium; L, low); T (°C), temperature.
[b]According to calibration by *Barker and Pawlewicz* [1994].

1. Crystals were buried to temperatures higher than the PAZ (i.e., > ~120°C), inducing a complete reset of the thermochronometer (provided that they remain during a long enough time above this temperature). The individual apatite single-grain ages are then younger than the stratigraphic age of the sample and generally form a single, low standard deviation group (Figure 7b). Apatite fission track results therefore describe the inversion history of the basin. However, in a sample that contains apatite crystals with strongly different annealing properties (i.e., issued from different sources), the dispersion can increase in relation to the residence time in the PAZ during postannealing cooling.

2. Crystals were buried to less than 60°C and not reset. The thermochronological signal then corresponds to their cooling history in the source area. On a radial plot (Figure 7b), the single-grain ages are older than (or equal to) the stratigraphic age of the sample and are generally widely scattered. The age dispersion reflects the diversity of the cooling ages of the source area, with several age populations usually revealed by statistical analysis. The central age for a sample with overdispersion is generally an average of the single-grain ages and without direct geological significance.

3. Crystals were buried to temperatures corresponding to the PAZ and partially reset. The single-grain ages are dispersed around the stratigraphic age of the sample (Figure 7b). The age dispersion is due either to the diversity of the cooling ages in the source area or to an important variability of the annealing rates of the individual grains (depending on their individual chemical composition) that can be highlighted by D_{par} measurements. The central age is a mixed age without geological significance, integrating source area cooling ages and the age at which the sediment exited the PAZ in the inverted basin.

4.1.3. Sampling Strategy and Sample Location

Samples for thermometry and AFT analyses were selected in order to constrain the burial and denudation history of the Jaca and NW Ainsa basins. Twenty-two samples were collected in the basin fill, from the base of the Hecho Group to the top of the Campodarbe Group. Thermometry measurements were also made on 16 of these samples. Seven additional samples for thermochronology were taken from the Paleozoic basement of the Axial Zone. Sample locations are shown in Figure 2 and are projected onto the cross section in Figure 5 according to their stratigraphic and structural locations and altitude (except OR14 and OR20 which are shown 1000 m higher than their actual altitude due to a lateral change of the Ordesa thrust geometry). Sample stratigraphic positions are indicated in Figure 10 where the samples from the Hecho Group turbidite succession are localized using the stratigraphic subdivisions ("turbidite systems") of *Remacha et al.* [2003] and *Caja et al.* [2009].
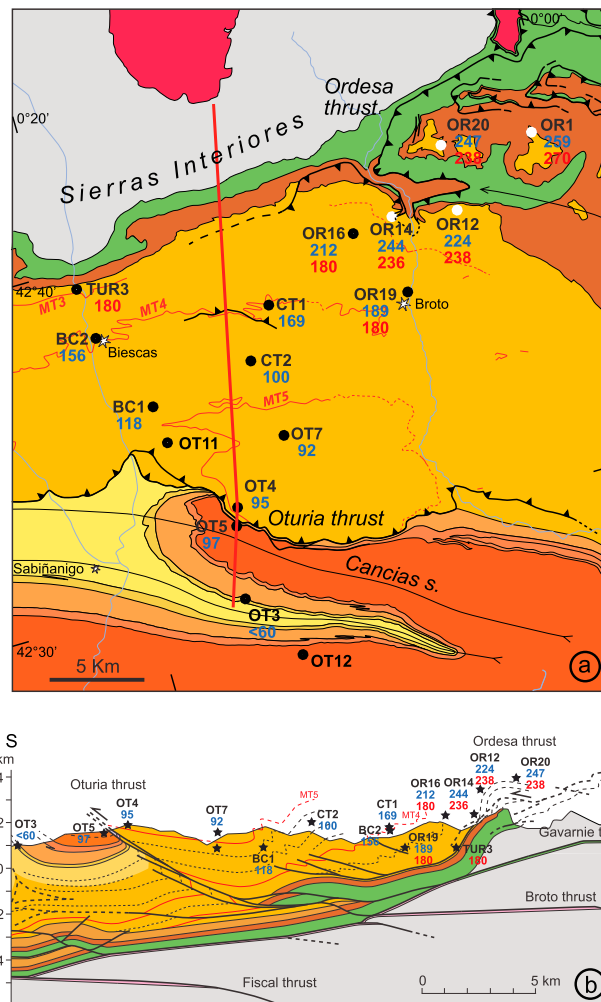
Figure 8. (a) Detail of map in Figure 2 and (b) detail of cross section in Figure 5 showing the distribution of maximum paleotemperatures in the Hecho Group turbidites of the northeastern Jaca Basin, deduced from vitrinite reflectance measurements (numbers in blue) and Raman spectroscopy of carbonaceous material thermometry (numbers in red). Complete analytical results and temperature interpretation are in Table 1. The stratigraphic position of samples is shown in Figure 10.

4.2. Thermometry Results
4.2.1. Vitrinite Reflectance Results

Measurements of vitrinite reflectance were made on 12 samples distributed across the whole Hecho Group turbidite succession and three samples in Priabonian to Rupelian sediments in the footwall of the Oturia thrust. Results are given in Table 2, and corresponding maximum paleotemperatures are reported in Figure 8. Except in one case, the result quality is moderate to good.

The Hecho Group samples show a marked decrease in vitrinite reflectance/maximum temperatures from bottom to top of the succession. Samples from the lowermost part (samples OR1, OR12, OR14, and OR20 from the Figols turbidite system), collected in the Ordesa valley (southern flank of the Monte Perdido massif), yield reflectance values between 2.98% and 4.54%, corresponding to temperatures comprised between 224 and 259°C according to the calibrations of *Barker and Pawlewicz* [1994]. Higher in the succession, the reflectance (temperature) values decrease to (i) 1.93 to 2.58% (189 to 212°C) in the Broto turbidite system (samples OR16 and OR19), (ii) to 1.28 to 1.51% (156 to 169°C) in the lower part of the Cotefablo turbidite system (samples BC2 and CT1), and (iii) to 0.64 to 0.8% (100 to 118°C) in the upper part of the Cotefablo turbidite system (samples CT2 and BC1). The lowest reflectance values are found at the top of the succession, where the samples yield values of 0.60 and 0.58%,

OT4 (Banaston turbidite system) and OT7 (Jaca turbidite system) respectively, corresponding to temperatures of 95°C and 92°C.

Sample OT5, in the Priabonian Santa Orosia conglomerate (lower Campodarbe Group) a few tens of meters below the Oturia thrust, has a reflectance value of 0.62% (97°C), similar to that of sample OT4 located 200 m above the thrust. In contrast, although being located about 1500 m lower in the succession, sample OT3 in the Bartonian Sabiñánigo sandstone yields a lower value of 0.35% (<60°C). Further to the south, sample SE5 corresponds to the youngest Campodarbe sediments preserved in the Guarga syncline on the studied section and has also a low reflectance value of 0.43% (68°C).

4.2.2. Raman Spectroscopy of Carbonaceous Material Results

The geothermometry approach of RSCM was conducted on 10 samples located in the stratigraphically lower turbidites. Characteristic spectra are shown in Figure 9, results are summarized in Table 2, and corresponding maximum paleotemperatures are reported in Figure 8.

The obtained spectra are composed of two broad bands, so-called D and G [e.g., *Wopenka and Pasteris*, 1993; *Yui et al.*, 1996], located at ~1350 cm^{-1} and ~1600 cm^{-1}, respectively. The analysis of band widths reveals variations with increasing CM thermal maturity, i.e., when going downward in the stratigraphic column:
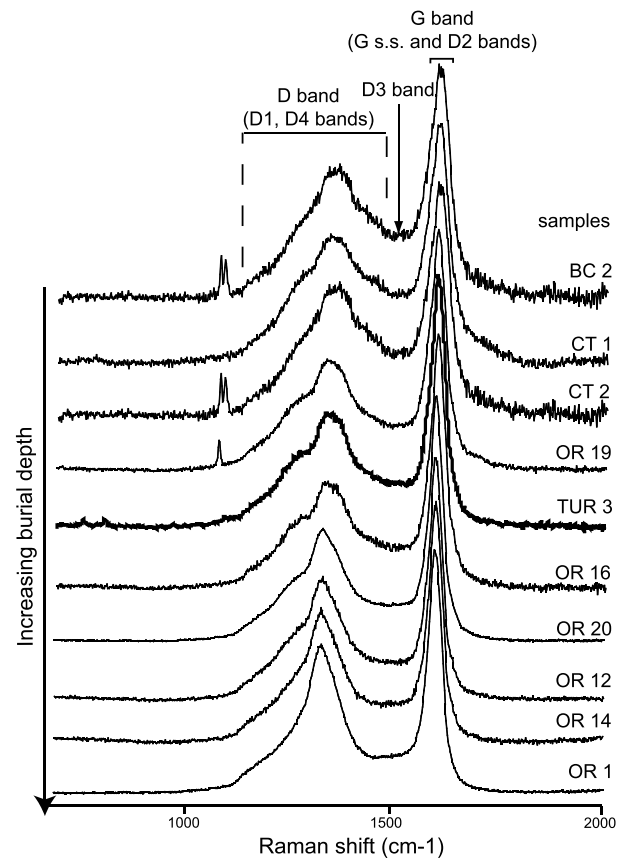
Figure 9. Characteristic spectra obtained for 10 samples (located on Figure 2) by Raman spectroscopy of carbonaceous material. See text for interpretation.

1. The width of the G band (including the G band stricto sensu and the D2 defect band) decreases before becoming almost constant when T exceeds ~200°C, i.e., from sample OR20 downward in Figure 9.

2. The width of the D band progressively decreases due to a gradual disappearance of defect bands such as the D4 band. The D band comprises at least two bands: the main defect band D1 located at ~1350 cm^{-1} and the D4 band, located at ~1200 cm^{-1} as a shoulder on the D1 band.

Samples OR1, OR14, OR12, and OR20 from the base of the Hecho Group (Figols turbidite system) in the Ordesa valley are characterized by Raman spectra indicating maximum paleotemperatures of 274°C, 262°C, 238°C and 211°C, respectively, with uncertainty of ± 25°C. However, sample TUR3 also located at the base of the succession 20 km to the west yields spectra indicating a lower temperature peak, of ~180°C. Further up in the stratigraphic column, the spectra of samples OR16 and OR19 (Broto turbidite system) also indicate temperature peaks of ~180°C, and those of samples CT1, CT2, and BC1a (Cotefablo turbidite system) record temperature peaks lower than 160°C.

4.2.3. Synthesis of Thermometry Results in the Hecho Group Turbidites

Thermometry shows maximum paleotemperatures decreasing upward across the Hecho Group turbidite succession, with a good first-order correlation (within the uncertainty margin) between temperatures deduced from the RSCM method and those deduced from vitrinite reflectance for temperatures >160°C (Figure 8). The highest temperatures are found at the base of the succession near the Ordesa valley, with mean values by both methods around 240°C (samples OR1, OR12, OR14, and OR20). Temperatures rapidly decrease to around 180–200°C about 1000 m higher in the stratigraphic column (samples OR16 and OR19). This result points to a high geothermal gradient around 50°C/km for the lower part of the succession in the Ordesa-Broto area (54°C/km if we compare the mean of temperature values obtained for samples OR16 and OR19 with those obtained for samples OR1, OR12, OR14, and OR20). However, this temperature distribution is specific to this area as a temperature of only about 180°C is found 20 km to the west at the base of the succession (sample TUR3), i.e., in a stratigraphic position equivalent to that of the higher-temperature Ordesa samples. Higher up section, the temperature decreases progressively to 90–95°C (vitrinite reflectance data) in the uppermost turbidites in the hanging wall of the Oturia thrust (samples OT4 and OT7). Gradients calculated using the stratigraphic thickness remain higher in the eastern part of the study area (about 35°C/km between samples OR16–OR19 and OT7) than in the western part (about 25°C/km between samples TUR3 and OT4). Although these calculations must be taken with caution due to the large uncertainties attached to the paleotemperature estimations and the relatively large distances between sampling sites, they point to a nonhomogeneous temperature distribution with a high gradient at the base of the turbidite succession in the northeastern part of the study area and much lower gradients in the western area and the upper part of the succession. These results are in general agreement with those of *Izquierdo-Llavall et al.* [2013] who studied the paleothermometry of the northern Jaca Basin using a combination of fluid inclusions, illite content in

Table 3. Apatite Fission Track Thermochronology Results

Sample[a]	Latitude	Longitude	Altitude (m)	N	$\rho d \times 10^5$ (Counted)	$\rho d \times 10^5$ (Counted)	$\rho d \times 10^5$ (Counted)	[U] (ppm)	$P(\chi^2)$	var (%)	Central Age $\pm 2\sigma$ (Ma)	D_{par} (μm)
BA1	N42°50′20″	W0°17′25″	3137	20	14.14 (8282)	2.24 (136)	18.52 (1123)	14.9	42.45	1	29.3 ± 2.7	2.10
BA5	N42°51′29″	W0°17′22″	2080	20	13.47 (8282)	1.82 (74)	15.08 (611)	13.87	100	1	27.9 ± 3.5	1.9
BA8	N42°45′15″	W0°14′22″	1614	20	13.87 (8282)	2.43 (156)	28.13 (1806)	24.51	98.06	0	20.5 ± 1.8	2.10
GV2	N42°42′39″	W0°03′25″	2212	23	13.63 (12,288)	3.4 (172)	25.84 (1308)	22.69	34.46	14	29.6 ± 2.6	_
GV5	N42°43′60″	W0°00′32″	1388	18	12.34 (10,996)	6.05 (245)	66.82 (2706)	64.3	97.53	0	18.2 ± 1.2	2.00
JA2	N42°47′45″	W0°31′27″	1632	20	10.92 (7145)	1.95 (91)	13.58 (634)	17.72	93.19	2	26.8 ± 3.1	_
JA3	N42°47′60″	W0°31′15″	1641	16	11.27 (7373)	4.18 (156)	29.1 (1087)	32.67	1.85	26	30.0 ± 3.5	_
TUR3	N42°39′26″	W0°19′18″	960	12	12.04 (12,288)	3.98 (32)	30.78 (248)	29.67	51.73	0	25.3 ± 4.8	_
OR1[b]	N42°40′09″	W0°00′52″	2580									
OR12[b]	N42°38′11″	W0°03′38″	2120									
OR14[b]	N42°38′49″	W0°06′53″	1230									
OR16	N42°33′37″	W0°08′43″	2281	31	11.22 (11,307)	4.9 (217)	35.64 (1580)	38.87	93.59	0	25.1 ± 1.9	2.32
OR19	N42°36′36″	W0°07′10″	918	43	13.74 (12,632)	3.45 (257)	33.33 (2480)	30.49	84.61	0	23.2 ± 1.6	_
OR20[b]	N42°40′35″	W0°04′53″	2848									
CT1	N42 37′30″	W0°12′21″	1700	18	8.86 (9558)	4.56 (115)	23.99 (606)	27.02	58.86	6	27.5 ± 2.9	_
CT2	N42°35′49″	W0°13′49″	1997	20	11.98 (12,632)	3.52 (198)	26.1 (1470)	28.59	71.1	0	26.3 ± 2.0	2.39
BC1	N42°35′28″	W0°18′36″	859	12	13.3 (7978)	0.55 (29)	4.54 (238)	3.85	98.19	0	27.7 ± 5.5	_
OT3	N42°29′25″	W0°16′56″	896	44	8.68 (9101)	8.5 (518)	28.62 (1744)	37.4	7.94	16	43.7 ± 2.7	_
OT4	N42°32′04″	W0°16′06″	1920	40	7.83 (9101)	4.72 (293)	17.11 (1063)	26.45	89.71	2	35.2 ± 2.4	_
OT5	N42°31′37″	W0°16′22″	1635	38	10.37 (9101)	4.92 (794)	21.01 (3389)	30.2	0.02	25	42.5 ± 2.7	1.49
OT7	N42°33′23″	W0°13′15″	1550	27	9.95 (9101)	4.7 (234)	18.6 (925)	30.93	4.31	27	41.5 ± 4.0	1.35
OT11	N42°34′26″	W0°17′56″	875	17	14.11 (12,632)	2.59 (84)	28.64 (929)	23.37	99.97	0	20.8 ± 2.4	2.49
OT12	N42°26′53″	W0°15′09″	1503	22	11.61 (12,632)	2.33 (174)	12.3 (920)	16.77	10.26	20	37.1 ± 3.6	_
SE1	N42°18′22″	W0°21′31″	963	40	11.86 (11,266)	4.79 (319)	19.82 (1321)	18.91	0.31	33	48.1 ± 4.2	_
SE5	42°23′45″	W0°23′34″	815	18	12.26 (12,632)	5.28 (109)	24.17 (499)	20.92	2.47	32	52.2 ± 7.5	2.57
AS1	N42°36′49″	E0°0.4′29″	2100	11	10.19 (10,996)	2.90 (36)	18.73 (232)	25.27	57.84	8	26.0 ± 4.7	_
AS3	N42°34′54″	E0°06′24″	1499	18	11.98 (10,996)	4.18 (108)	25.57 (661)	11.98	14.1	11	32.5 ± 3.6	_
AS5	N42°31′21″	E0°07′57″	863	10	11.62 (10,996)	3.89 (60)	25.85 (399)	28.6	95.55	0	28.5 ± 4.0	_
AS6	N42°24′13″	E0°08′55″	554	39	10.88 (11,582)	4.43 (290)	31.85 (2086)	38.61	98.52	0	28.4 ± 1.9	_

[a]Samples are located on the map in Figure 2, projected on the cross section in Figure 5 and located against the stratigraphy with AFT result diagrams in Figure 10; N, number of grains; ρd, standard track density; ρs and ρl, spontaneous and induced track densities, respectively; $P(\chi^2)$, probability of c2 for v degrees of freedom (where v is number of crystals minus 1).
[b]Samples OR1, OR12, OR14, and OR20 did not provide apatite grains suitable for AFT analysis but were used for thermometry measurements (Table 2).

mixed illite-smectite layers, Kübler index, and vitrinite reflectance data. Although their data are scarce in the area studied here and the paleotemperatures obtained are slightly lower than ours, their results confirm the elevated temperatures at the base of the turbidite succession in the Ordesa area (Rr% of 1.89 close to our OR16 sample) and relatively lower temperatures in the same stratigraphic position more to the west (Rr% of 1.32 close to our TUR3 sample).

Hence, the very high temperatures found at the base of the Hecho Group turbidites at Ordesa appear as an anomaly both from the high thermal gradient they imply in the lowermost part of the succession, unexpected in this foreland basin context, and from the fact that a lower temperature is found laterally in an equivalent stratigraphic position. Below, we discuss the possible origin of these elevated temperatures (section 4.4) and refine inferences on geothermal gradients using the structural restoration (section 5).

4.3. Apatite Fission Track Results

The results are reported in Table 3, and diagrams of fission track analytical data versus stratigraphic position are presented in Figure 10. Figure 11 summarizes the evolution of the AFT central ages and mean ages of the main statistical single-grain age populations for the various samples according to depositional ages. The D_{par} measurements performed on selected samples are presented in Figure 12.

4.3.1. Axial Zone

Result from the Axial Zone are presented in Figure 10a.

Granite samples GV5, from the Gavarnie thrust footwall, is fully reset with a central age of 18.2 ± 1.2 Ma. Granite samples BA1, from the top of the Gavarnie thrust hanging wall culmination, and BA5 and BA8,
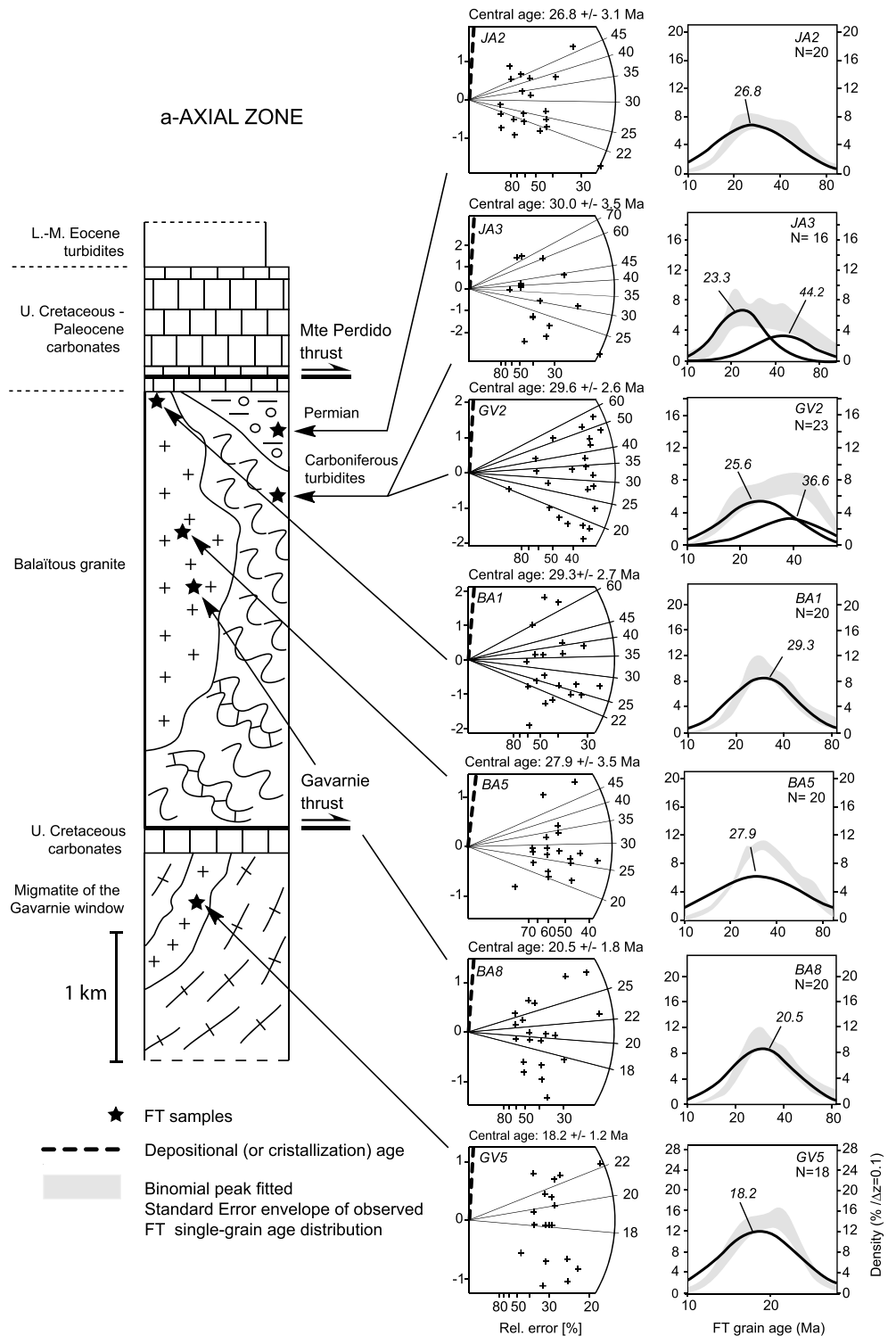
Figure 10. Apatite fission track data from the Axial Zone (a), the Hecho Group turbidites in the Jaca and Ainsa basins (b and c, respectively) and the Guarga syncline (d). Data are expressed as radial diagrams (central column) [*Galbraith*, 1990] and corresponding statistical decomposition of single-grain age distribution into a set of component distributions with the BinomFit® software (right column) [*Brandon*, 2002], using the binomial "peak-fitting" method of *Galbraith and Green* [1990] and *Galbraith and Laslett* [1993]. Dashed lines in the radial diagrams indicate either the sample depositional age (for sediments) or crystallization age (for granitic rocks). Apatite fission track results are plotted against a synthetic stratigraphic column of the Axial Zone and Jaca Basin (modified from *Caja et al.* [2009] for the Hecho Group turbidites). The stratigraphic position of samples from the Ainsa Basin (Figure 10c) is plotted at the equivalent position on the stratigraphic column in Figure 10b. Samples are located in Figures 2, 5, and 8.
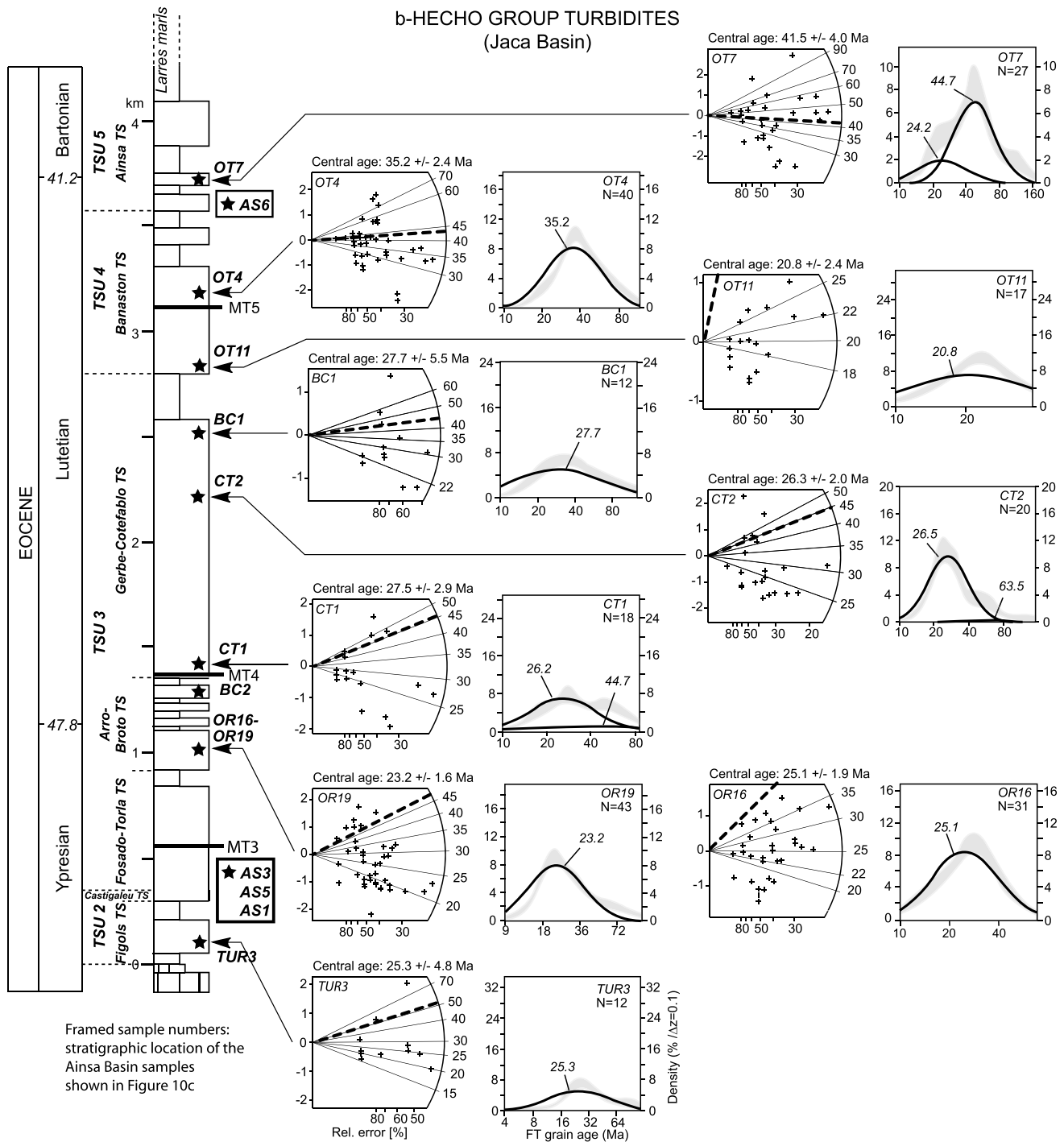
Figure 10. (continued)

situated some 1000 m and 1500 m below, respectively, are again fully reset with central ages of 29.3 ± 2.7 Ma, 27.0 ± 3.5 Ma, and 20.5 ± 1.8 Ma, respectively.

Paleozoic samples GV2, JA2, and JA3, from the toe of the Gavarnie thrust sheet, have central ages ranging between 26.8 ± 3.1 Ma and 30.0 ± 3.5 Ma. Sample JA3 displays a significant dispersion of the single-grain ages (var% = 26 and $P(\chi^2) = 1.8$; Table 3) which are all much younger than the stratigraphic age. Sample GV2 also shows a significant dispersion (var% = 14) but did not fail the χ^2 test (Table 3). Statistical analysis shows the existence, in samples GV2 and JA3, of two age populations in which the major one (i.e.,
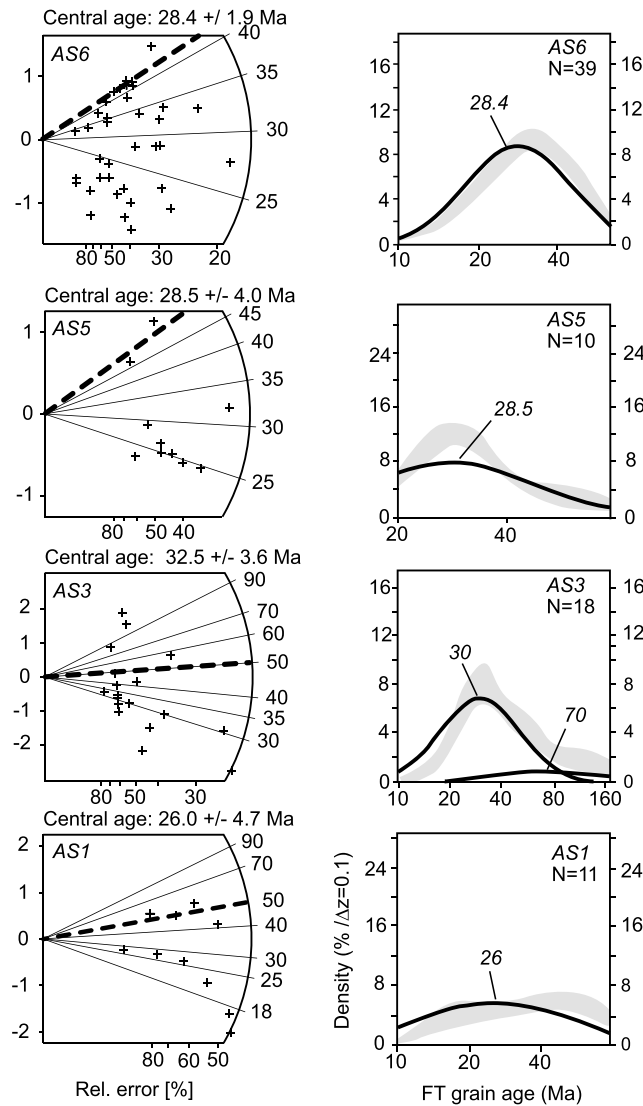
c-HECHO GROUP TURBIDITES
(Ainsa Basin)

Figure 10. (continued)

corresponding to the majority of the single-grain ages) has a mean age of 25.6 Ma (GV2) and 23.3 Ma (JA3). Sample JA2 presents only one age population. The fact that in the three samples, the single-grain ages are all much younger than the Paleozoic stratigraphic ages argue for a total resetting. The strong dispersion of the single-grain ages in sample JA3 and, to a lower extend in sample GV2, could be explained by the high number of inclusions within the crystals that lead to errors in age determination. The cooling ages of samples GV2 and JA3 are therefore likely to correspond to the age of the main age populations, i.e., 25.6 Ma and 23.3 Ma, respectively. These are consistent with the cooling age of 26.8 ± 3.1 Ma obtained for sample JA2.

4.3.2. Hecho Group Turbidites

Result diagrams from the Hecho Group turbidites are presented in Figures 10b and 10c for the Jaca and Ainsa basins, respectively. These samples provided few apatite crystals with low track numbers linked to low ^{238}U content.

In the Jaca Basin, samples OR1, OR12, OR14, and OR20 from the base of the succession (Figols turbidite system), collected around the Ordesa valley (Figure 2), could not be analyzed due to the very low number and bad preservation of apatite crystals. Sample TUR3 collected at the same stratigraphic level more to the west (Figure 2) contained apatite crystals that yielded a central age of 25.3 ± 4.8 Ma, much younger than the stratigraphic age (~50–51 Ma)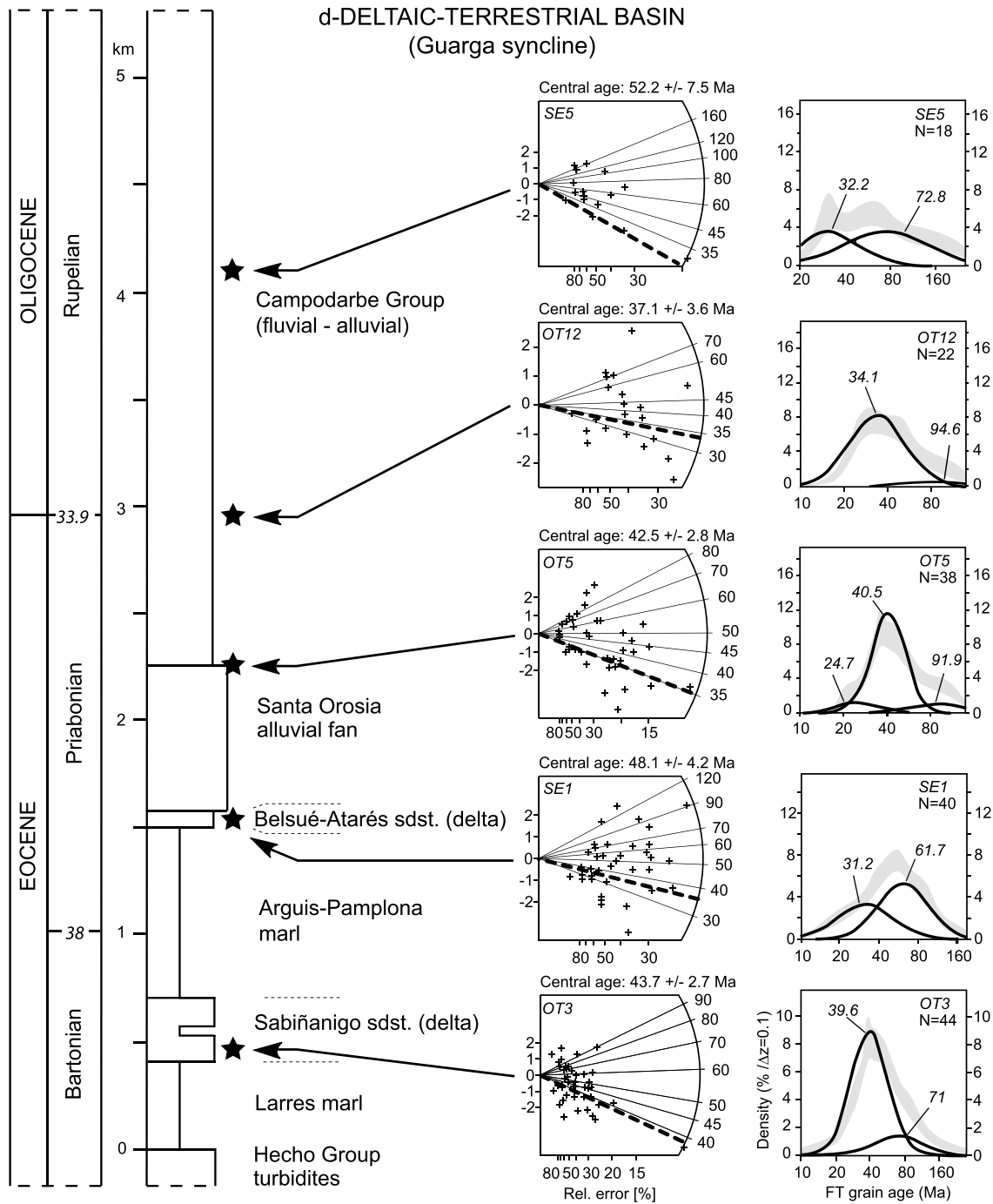. Although a few single-grain ages older than 50 Ma could suggest that the fission track reset might not have been total, the statistical parameters indicate a single age population confirmed by the BinomFit® model. Complete resetting is thus considered for sample TUR3.

Higher in the succession, samples OR16 and OR19 (Broto turbite system) have central ages of 25.1 ± 1.9 Ma and 23.2 ± 1.6 Ma, respectively. Although the calculated variance is very low and the samples did not fail the χ^2 test, single-grain ages form a relatively dispersed single population (especially in OR19), with most of the ages spanning from close to the stratigraphic age (~49–50 Ma) to around 15–20 Ma (early Miocene). The unimodal single-grain age distributions, associated to the scattering of the ages up to the stratigraphic ages suggest major but possibly not total reset.

The central ages of samples TUR3, OR16 and OR19 are similar to the exhumation ages observed in the Paleozoic samples of the Gavarnie thrust sheet (GV2, JA2, and JA3; Figure 10a), further attesting to a probable near total reset. Based on this observation, the central ages of these samples can be considered as close to the exhumation age.

Figure 10. (continued)

Further south and stratigraphically higher, samples CT1, CT2, and BC1 (Cotefablo turbidite system) have central ages ranging between 26.3 ± 2.0 Ma and 27.7 ± 5.5 Ma. Like samples OR16 and OR19, they all have a low statistical dispersion and passed the χ^2 test (Table 3). However, the single-grain ages are scattered from around the stratigraphic age (~48–49 Ma) to early Miocene ages. The BinomFit® model identifies a major population in samples CT1 and CT2, with mean ages of 26.2 and 26.5 Ma, respectively, associated to a very minor population with mean ages of 44.7 and 63.5 Ma, respectively. The occurrence of two statistically distinct age populations in samples CT1 and CT2 suggests that full resetting was possibly not reached, although the central age can be considered has close to the exhumation age. Only one population is statistically
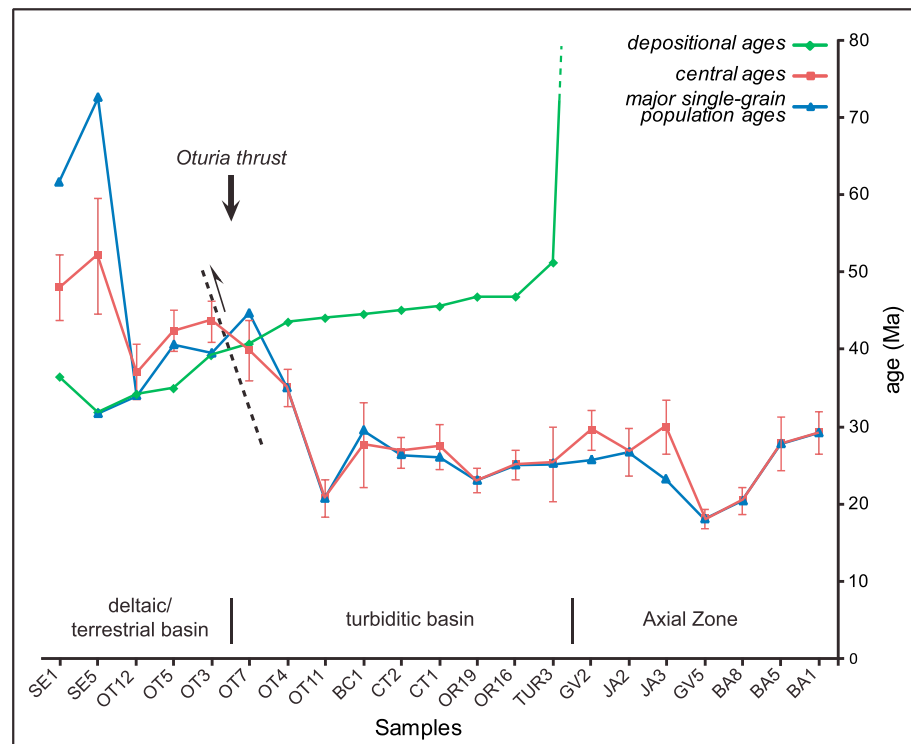
Figure 11. Diagram showing the evolution of sample depositional ages, apatite fission track central ages, and mean ages of the statistically most representative single-grain age population in the N-S transect of the study area (see sample location in Figures 2, 5, and 8, and apatite fission track data in Figure 10).

defined in BC1. Stratigraphically close to BC1, sample OT11 has a much younger central age of 20.8 ± 2.4 Ma and a single age population.

Higher in the succession, sample OT4 (Banaston turbidite system) has a central age of 35.2 ± 2.4 Ma with single-grain ages scattered on both sides of the stratigraphic age (~43 Ma) although forming a single statistical population based both on the analytical parameters (Table 3) and on the BinomFit® model (Figure 10b). At the top of the turbidite succession, sample OT7 (Jaca turbidite system) has a central age of 41.5 ± 4.0 Ma, failed the χ^2 test ($P(\chi^2) = 4.3$) and shows a significant single-grain age dispersion (var% = 27), distributed on both sides of the stratigraphic age (~41 Ma). Two age populations can be extracted from sample OT7 using BinomFit®, the mean age of the major population being 24.4 Ma. Sample OT7 has clearly been partially reset, at a lower temperature (or during a shorter time) than the stratigraphically lower turbiditic samples. In particular, the statistical parameters calculated for sample OT7 and the observed two populations advocate for a lower reset level compared to sample OT4. However, the occurrence of single-grain ages much older than the stratigraphic age in sample OT4 (Figure 10b) also suggests partial reset in this sample.

In the Ainsa Basin, samples AS1, AS3, and AS5 have central ages ranging between 26.0 ± 4.7 Ma and 32.5 ± 3.6 Ma similar to the stratigraphically equivalent lower turbidites sampled in the Jaca Basin (TUR3, OR16, and OR19). Likewise, most single-grain ages are dispersed between close to the stratigraphic age and 15–20 Ma, with a few older ages in samples AS1 and AS3 that both show a higher statistical dispersion (var% = 8 and 11, respectively). In samples AS3 two age populations can be statistically distinguished using BinomFit® with a major population mean age of 30 Ma and a limited secondary population with a mean age of 70 Ma. In the upper part of the succession, sample AS6 has a central age of 28.4 ± 1.9 Ma with a low dispersion of the single-grain ages, forming a single statistical age population younger than the stratigraphic age.

Like their stratigraphic equivalents in the Jaca Basin, samples AS1, AS3, and AS5 suffered a strong reset. Their AFT central ages are consistent with those obtained in the Jaca Basin and can thus be considered as close to the exhumation age. Sample AS6, situated further up section is notably younger than its stratigraphic equivalent (OT7) in the Jaca Basin, which may either indicate lateral variation in exhumation time or different annealing behavior.
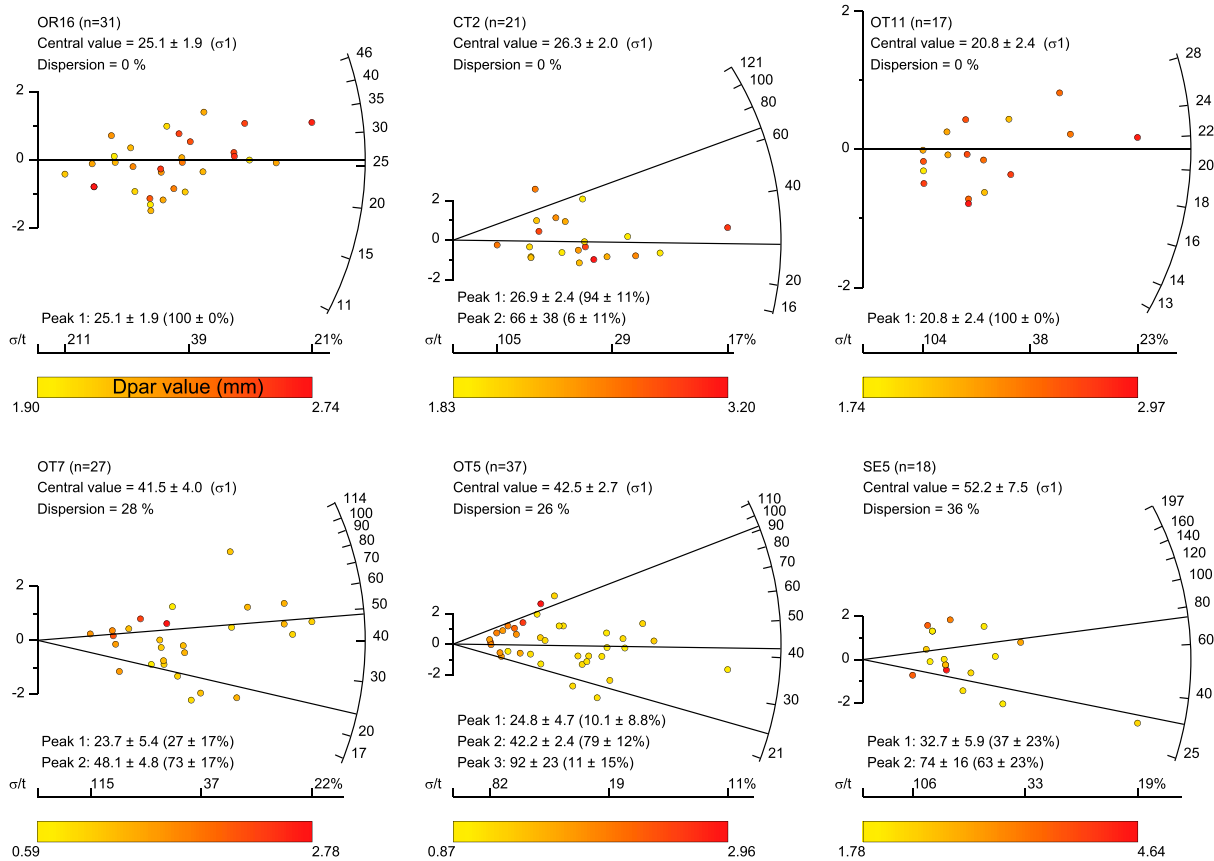
Figure 12. Radial plot diagrams [*Galbraith*, 1990] showing the relation between the D_{par} value and apatite single-grain ages in a selection of strongly to totally (OR16, CT2, and OT11) and partially to not/very weakly reset (OT7, OT5, and SE5) samples. Each D_{par} value corresponds to the mean value of 20 measurements. The n is the total number of analyzed apatite crystals; central value is the central AFT age for the sample; peak is the central value of individual grain populations within the sample, calculated using a mixture modeling [e.g., *Galbraith and Green*, 1990]. Minor differences between the peak values and the age of populations indicated in Figure 10 are due to data rounding in the BinomFit software [*Brandon*, 2002]; s/t represents the error (in % of the grain age) for each single grain. Graphs have been obtained using the Density Plotter 6.3 software of *Vermeesch* [2012]. See sample location in Figures 2, 5, and 8 and apatite fission track data in Figure 10.

4.3.3. Southern Jaca Basin

Results from the southern Jaca Basin are presented in Figure 10d.

In the footwall of the Oturia thrust, sample OT3 (Sabiñánigo sandstone) has a central age of 43.7 ± 2.7 Ma, older than the stratigraphic age (~39 Ma), a relatively important dispersion (var% = 16) and failed the χ^2 test $(P(\chi^2) = 7.9)$ (Table 3). The single-grain age distribution includes a large proportion of crystals older than the stratigraphic age. Two age populations are individualized using BinomFit®, the major one having a mean age of 39.6 Ma, equivalent to the stratigraphic age and the minor one having a mean age of 71 Ma. In the same structural unit but higher in the succession (Santa Orosia conglomerate, lower Campodarbe Group), samples OT5 and OT12 have central ages of 42.5 ± 2.7 Ma and 37.1 ± 3.6 Ma, respectively, older than their stratigraphic age (~34–35 Ma). They both show a significant single-grain ages dispersion (Var% = 25 and 20 respectively) and sample OT5 failed the χ^2 test (P(χ^2) = 0). In both samples, a large proportion of single grain ages are older than the stratigraphic age except a group of younger ages between ~35 and 20 Ma. In sample OT5, three age populations are distinguished using BinomFit® with the major population having a mean age of 40.5 Ma. Similarly, in sample OT12, two populations are distinguished with the major one having an age of 34.1 Ma.

Further south, in the Guarga syncline, sample SE5 (top of the Campodarbe Group) has a central age of 52.2 ± 7.5 Ma with a strong dispersion (var% = 32) and failed the χ^2 test (P(χ^2) = 2.5) (Table 3). The single-grain ages are all older than, or close to, the stratigraphic age (≈ 30 Ma). Two statistical age populations are distinguished using BinomFit®, the major one having a mean age of 72.8 Ma.

In the Sierras Exteriores, sample SE1 (Belsué-Atarés sandstone) has a central age of 48.1 ± 4.2 Ma with a significant single-grain ages dispersion (var% = 32) and failed the χ^2 test ($P(\chi^2) = 0$) (Table 3). Two age populations can be statistically extracted using BinomFit®, with a mean age of 61.7 Ma for the main one. Hence, all the samples situated in the footwall of the Oturia thrust (OT3, OT5, OT12, SE1, and SE5) clearly show very weak or no resetting.

4.3.4. Summary of Thermochronology Results

In summary, basement samples in the Axial Zone are all totally reset. The lower-middle Eocene turbidite samples in the northern Jaca Basin display complete to moderate resetting with central ages younger than their stratigraphic ages. The lowest samples (TUR3, OR19, and OR16), which yield the youngest central ages (23–25 Ma), display a single age population indicating a high to complete reset level, suggesting burial to temperatures higher or close to the high-temperature limit of the PAZ. The late Oligocene (Chattian) central age of those samples can be considered as their exhumation age in the basin. Further up in the succession, the possible occurrence of several age populations calculated using BinomFit® in samples CT1 and CT2 may reflect a lower, however, strong level of resetting. Considering the still high reset level and the coherence with the central ages of the lowest samples, the Chattian central ages of those samples can again be estimated as close to the exhumation age. At the top of the turbidite succession, the two age populations expressed in sample OT7, associated with a central age equivalent to the stratigraphic age clearly indicate partial resetting. The central ages of the sample can no longer be taken as indicative of exhumation. Finally, all the upper Eocene-lower Oligocene deltaic/terrestrial sediments in the southern Jaca Basin are not/very weakly reset with central ages older (up to the Late Cretaceous) than their stratigraphic age. The Oturia thrust marks the limit between the partially reset part of the basin in the hanging wall and the nonreset part in the footwall. As illustrated in Figure 11, the central ages increase southward and stratigraphically upward across the Jaca Basin, reflecting the progressive decrease of reset level. It is also important to note that, all along the section, there is no correlation between the reset level and the sample topographic elevation. Finally, all the samples analyzed show an absence of correlation between the D_{par} of single grains and the statistically identified single-grain age populations (Figure 12), suggesting that the single-grain age dispersion is controlled by the complex thermal history of each crystal rather than by their annealing properties. For partially or nonreset samples, the observed dispersion of apatite single-grain ages reflects the variability of the thermal history of the sediment sources.

4.4. Comparison of Thermometry and Thermochronology Results

We have seen above that the high maximum paleotemperatures found in the lowest part of the Hecho group turbidites suggest the existence of a thermal anomaly. These high temperatures also show noticeable discrepancies with the thermochronology data. As discussed above, a complete reset of the AFT system in samples TUR3, OR19, and OR16 can be envisaged. However, while the thermometry derived maximum temperatures >180°C obtained in these samples are compatible with a high degree of reset, they should have led to a tighter clustering of the individual ages around the exhumation age (i.e., around 20 to 25 Ma). Similarly, with thermometry derived maximum temperatures around 170°C, the AFT system in sample CT1 should have been completely reset, not allowing for two statistical populations as calculated using BinomFit® (Figures 8 and 10b) [*Galbraith*, 2005].

In order to further test the compatibility between the thermochronology and thermometry results, we performed inverse modeling of the dataset for samples OR16, CT2, and SE5 representing, respectively, the deep, intermediate, and shallow parts of the sedimentary sequence. Modeling was done using the QTQt software [*Gallagher*, 2012]. In a first set of models (Figures 13a, 13c, and 13e), the input parameters were the individual grain ages, the mean D_{par} value of the sample, the vitrinite reflectance value, and the estimated stratigraphic age of the sample. A second run (Figures 13b, 13d and 13f) further included a temperature—time box corresponding to the vitrinite-derived temperature (Table 2) at the estimated time of maximum burial (with an error margin of ± 10 Ma). This last constraint was introduced to force the model to reach the vitrinite-derived temperature. Sample OR16 (Figures 13a and 13b) clearly reached temperatures higher than the PAZ (around 170°C), the predicted AFT age being similar to the observed one. This is consistent with both the calculated Raman temperature of 180°C and a total reset of the sample as suggested by the single age distribution and the central fission track age (Figure 10b). However, the predicted vitrinite value (1.5 to 1.6%) is clearly lower than the observed one (2.58%), even when the model is forced to pass through the high-temperature
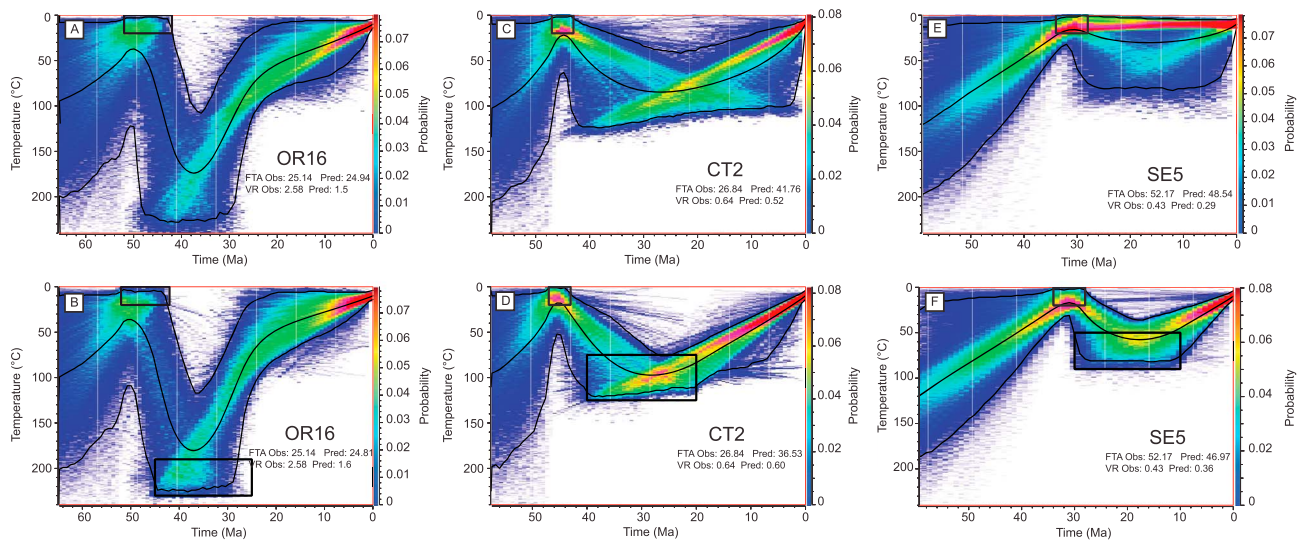
Figure 13. Statistic inverse modeling of the AFT and vitrinite reflectance data for three selected samples from the Jaca Basin. Models were obtained using the QTQt software [*Gallagher*, 2012]. The temperature-time constraints are indicated by black rectangles and correspond to the estimated stratigraphic age of the sample in a (a, c, and e) first set of models, complemented by the vitrinite-derived temperature at the estimated time of maximum burial (with an error margin of ± 10 Ma) in a (b, d, and f) second set. The black line represents the mean expected model cooling curve [*Gallagher*, 2012], and the blue to red color scale describes the probability of the cooling curve to pass through a given temperature-time point. FTA Obs is the observed AFT central age, and FTA Pred is its predicted value; VR Obs is the observed vitrinite reflectance value, and VR Pred is the value predicted by the model. See text for discussion.

constraint. This last result further supports an anomalous vitrinite reflectance value. Sample CT2 (Figures 13c and 13d) clearly remained below the high-temperature limit of the PAZ, reaching a maximum temperature around 100°C in both models. The predicted age is higher than the observed one, which is consistent with partial annealing in a multisourced detrital sample (the predicted annealing behavior of the individual grains is governed by the mean D_{par} value used as input parameter while the observed age represents strongly variable kinetics due to D_{par} values ranging between 1.83 and 3.20; Figure 12). The predicted vitrinite values of 0.52 to 0.60% are consistent with the observed one (0.64%). Altogether these results suggest that sample CT2 indeed reached a burial temperature of about 100°C. Finally, sample SE5 (Figures 13e and 13f) clearly remained above the PAZ as suggested by the multimodal single grain AFT age distribution and the central AFT age much older than the stratigraphic age (Figure 10d). The predicted vitrinite reflectance value is close to the observed one (especially in the second model), and the vitrinite-derived temperature of 68°C, while slightly high, is consistent with both the maximum temperature reached by the models and the low degree of reset suggested by the single grain AFT age distribution.

The anomalously high geothermal gradient deduced at the base of the turbidite succession in the Ordesa valley is unexpected in a foreland wedge context. Although a high gradient (80°C/km) characterized the North Pyrenean Zone during the Late Cretaceous and was maintained after the beginning of the Pyrenean convergence (~83 Ma) until the onset of continental collision around 50 Ma [*Vacherat et al.*, 2014], the sedimentary sequence studied here was probably too far south (in a region of more "normal" geothermal gradient) and too young to have been notably affected by this high temperature. Temperature increase related to deformation (shear-heating) is also unlikely as (i) the high temperatures found in the lower turbidites are not specifically related to fault zones, (ii) the inferred mean strain rates in the wedge are low (see above), and (iii) the east-west temperature variations (e.g., between OR14 and TUR3; Figure 8) do not correlate to detectable differences of macroscopic deformation. By contrast, large amounts of fluids can flow across sedimentary wedges and hot fluids migrating over a relatively short time span can noticeably modify the local geothermal gradient and affect the thermometry and thermochronology systems [e.g., *McCulloch*, 1994; *O'Brien et al.*, 1999; *Arehart and Donelick*, 2006; *Tagami*, 2012]. In such cases, the behavior of the thermometry and low-temperature thermochronology systems is largely controlled by their kinetics, i.e., their capacity to react rapidly to temperature changes: the vitrinite system equilibrates very quickly [e.g., *Galushkin*, 1997; *Huang*, 1996; *Le Bayon et al.*, 2012] while the AFT system has a much slower kinetics. *McCulloch* [1994] shows that vitrinite reflectance data of Carboniferous rocks from eastern Ireland indicate maximum temperatures

greater than 150°C while AFT data record maximum temperatures of 80 to 110°C. The author explains this misfit by rapid fluid migration during early Tertiary uplift of the eastern Irish margin. Similarly, *O'Brien et al.* [1999] show that rapid brine migration in subbasins of the Timor Sea affected the AFT system only within the immediate vicinity of the faults. Furthermore, they calculate that for a fluid temperature of about 120° C, complete equilibration of the AFT system requires fluid flow duration of at least 1 Myr. In the Pyrenean case, on the basis of fluid inclusion and oxygen isotope data on calcite-quartz veins and of chemical data on synkinematic chlorite, *Lacroix et al.* [2011, 2012] report fluids with temperatures of about 200 to 240°C in the Monte Perdido thrust fault zones, which they relate to the activity of the Monte Perdido thrust system and to a speculative reactivation during the emplacement of the Gavarnie thrust. These temperatures are very similar to the maximum paleotemperatures obtained in this study for the base of the Hecho Group turbidite succession in the same area, in the hanging wall of the Monte Perdido sole thrust (the Ordesa thrust) but outside the fault zones (cf. samples OR1, OR12, OR14, and OR20 from the Ordesa valley; Figure 8 and Table 2). *Lacroix et al.* [2011, 2012] conclude that hot fluid migration was absent along the Monte Perdido fault zones from the study of the fault zones and their adjacent host rocks. In contrast, our results suggest that hot fluid migration may have occurred across the Hecho Group turbidites, not restricted to fault zones but probably along distributed fracture networks. Similarly, circulation of relatively hot fluids may have participated to the paleotemperatures around 95°C recorded by vitrinite reflectance both in the hanging wall and footwall of the Oturia thrust (samples OT4 and OT5, respectively) while sample OT3, located stratigraphically below OT5, records a lower temperature probably representing the burial temperature (Figure 8 and Table 2). Furthermore, the fact that anomalously high temperatures occur both in the synkinematic minerals in the Monte Perdido thrust fault zones and around the Oturia thrust while both structures have not the same age (see above) attests to distinct episodes of fluid migration across the Jaca Basin. An important implication of our results is that the high paleotemperatures in the Ordesa area cannot be used to derive a mean geothermal gradient related to burial, as attempted by *Lacroix et al.* [2011, 2012, 2014].

5. Evolution of the South Pyrenean Wedge

In what follows we integrate the structural, stratigraphic, thermal, and thermochronological data presented above in a thermotectonic evolution model of the western south Pyrenean wedge, illustrated in Figure 14 by the sequential restoration of the structural section of Figure 5. The steps selected for the restoration correspond to the end of the major basement thrusting stages, i.e., the Eaux-Chaudes (~38 Ma), Gavarnie (~33.5 Ma), Broto (~28 Ma), and Fiscal-Guarga (~20 Ma).

The foreland flexure at each stage was determined from the stratigraphic thickness of basin sediments, and the structures in the thrust wedge were geometrically restored according to the timing of tectonic activity discussed above and synthesized in Figure 4. The topography of the wedge is represented schematically as a smooth surface at an altitude with respect to the foreland basin surface of 1000 m at stage A and 1500 m at following stages, the latter value being analogous to the present-day one.

Stage A: Lutetian-Bartonian (ending at ~38 Ma). In the northern Axial Zone, the Eaux-Chaudes basement thrust is already active at least from the early Eocene. The Lutetian-Bartonian corresponds to the period of the propagation of the Eaux-Chaudes/Monte Perdido thrusting in the Jaca Basin, dated by growth strata on the Añisclo and Boltaña anticlines and contemporaneous with the deposition of the upper part of the turbidite succession and lower part of the overlying deltaic systems (Larrés marl and Sabiñánigo sandstone). While the Lutetian turbidites are fed from the east, the northern provenance of the uppermost turbidites, of early Bartonian age, is the first record in the basin of the tectonic uplift related to the Eaux-Chaudes thrusting [*Roigé et al.*, 2016]. On the studied section, the thrust front corresponds to the Ordesa thrust (laterally equivalent to the Añisclo and Boltaña anticlines), which splays upward in the northern part of the Hecho Group turbidite wedge, with development of chevron folding and related cleavage. To the south, the turbidites onlap the backstepping Paleogene limestone platform and are overlain by the Arguis-Pamplona marl, deposited directly above the Guara limestones in the Sierras Exteriores area. In this area, deformation begins in the early Bartonian with detachment folds, initially oriented NW-SE which progressively rotate clockwise during their growth. Figure 14a shows the Arguis anticline at an intermediate stage of development and rotation. Note that the growth of the N-S folds being related to lateral compression in the foreland of the Boltaña anticline, they are not rooted in the basement thrusts present in the studied section. In the north, the end of this stage
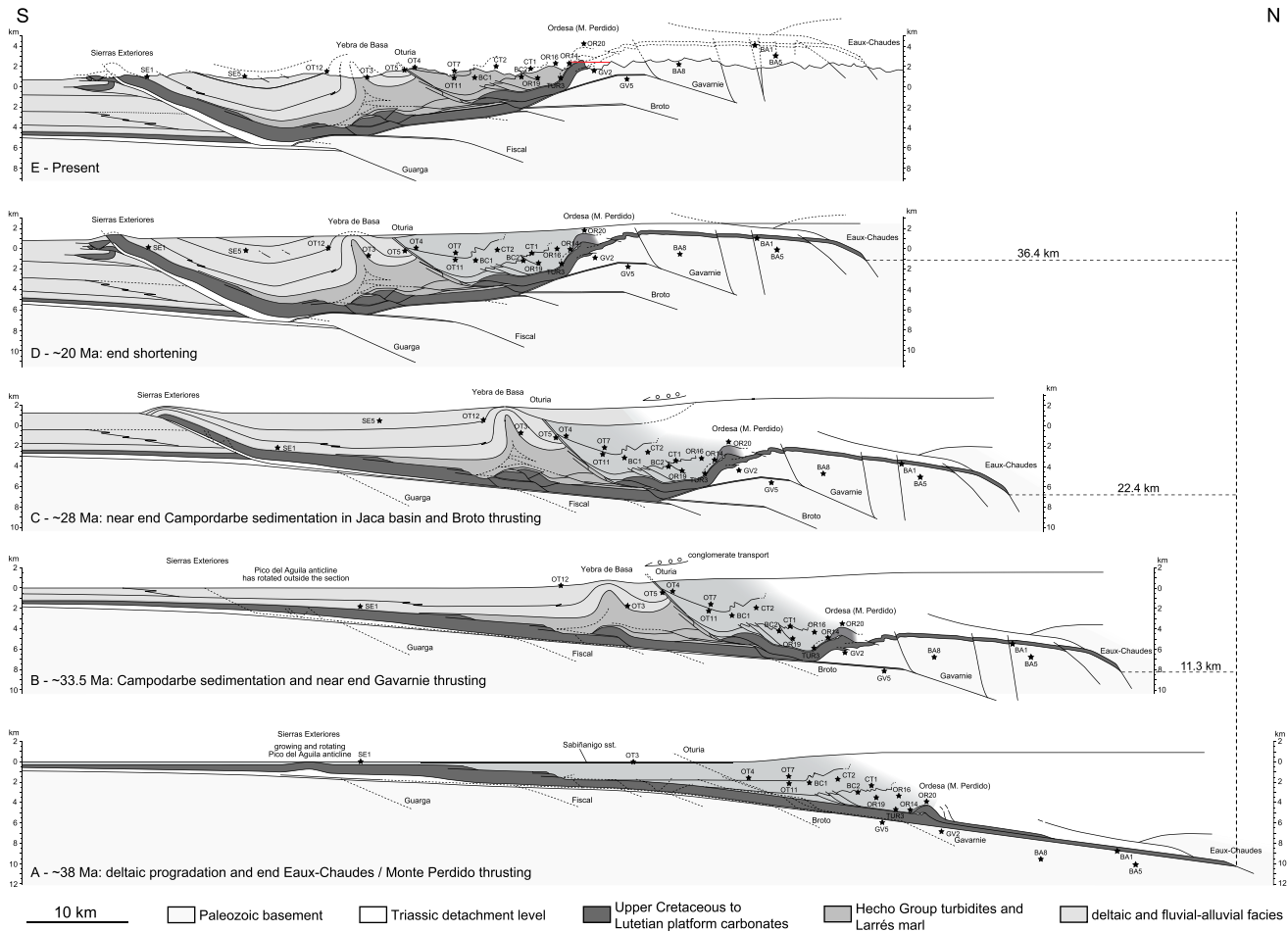
Figure 14. Model for the tectonic evolution of the eastern Jaca Basin and southern Axial Zone, corresponding to the sequential restoration of the cross section in Figure 5. See detailed legend in Figure 5.

corresponds to the Campodarbe unconformity at the crest of the Boltaña anticline (end Bartonian), but growth of the detachement folds of the Sierras Exteriores finishes during the early Priabonian (Figure 4). At the end of the stage, the deepest burial depth of turbidites is around 5500–6000 m at the front of the Ordesa thrust (samples OR14 and TUR3) while the top of the basement of the future Axial Zone is far below the lower limit of the apatite fission track PAZ (8000–10000 m, cf. samples GV2 and BA1).

Stage B: Priabonian (to earliest Rupelian; ending at ~33.5 Ma). The Priabonian stage corresponds to the Gavarnie thrusting, transferred into the basin to the Oturia and Yebra de Basa cover thrusts during the deposition of the Arguis-Pamplona marl, the Belsué-Atarés deltaic sandstone, and the lower part of the Campodarbe fluvial-alluvial deposits. Cleavage formation and chevron fold tightening probably continued during this stage at the front of the Gavarnie thrust hanging wall culmination [*Séguret*, 1972]. Abundant sandstone pebbles in the Campodarbe alluvial fans deposited in the Oturia thrust footwall (the Santa Orosia conglomerate) attest to uplift and erosion of the Hecho Group turbidites above the Gavarnie thrust hanging wall culmination [*Roigé et al.*, 2016]. These conglomerates accumulate above the active Yebra de Basa anticline which is in an intermediate stage of growth at the end of the stage. To the south, the growth and rotation of the N-S folds terminates during this stage. The Arguis anticline is no longer visible in Figure 14b as it has rotated out of the section. We cannot discard the possibility that a structure (detachment fold or thrust ramp) existed south of the N-S folds to accommodate the transition between the domain affected by the clockwise rotation and the undeformed foreland. However, the existence and nature of such a structure and the amount of N-S shortening that it may have accommodated remain highly speculative, and thus, it is not represented in Figure 14. While the turbidites above the uplifting Gavarnie thrust culmination are

eroded, the base of the turbidites on the southern edge of the proto-Axial Zone reaches a maximum depth close to 7000 m due to tectonic thickening and leading to complete reset of samples OR16, OR19, and TUR3. The top of the basement is uplifted in the culmination but remains deeply buried around 7000 m.

Stage C: Rupelian (ending at ~28 Ma). The Rupelian stage corresponds to the Broto thrusting and the deposition of the upper part of the Campodarbe Group. The Broto thrusting results in the late stage of the Yebra de Basa cover thrusting and the propagation of the frontal ramp in the Sierras Exteriores. Cross-section restoration shows that thick sediment accumulation in the basin during this stage implies that Rupelian conglomerates are also deposited north of the Oturia thrust, onlapping northward onto the already deformed hanging wall turbidites in a way similar to syntectonic conglomerates of the same age in the central Pyrenees [e.g., *Coney et al.*, 1996; *Babault et al.*, 2005]. It follows that in spite of tectonic uplift above the Broto thrust hanging wall culmination, most of the turbidites reach their maximum burial during this stage, although not much deeper than in the previous stage for samples in the northern area (7000 m for sample TUR3). Only the northernmost turbidite sample (OR20) begins to be exhumed. These burial depths of the turbidites are consistent with the total rest of the lowermost ones and the partial reset of the upper part of the succession attested by the QTQt modeling (Figure 13). In the Axial Zone, the top basement is slightly uplifted at burial depths between 7000 m (sample GV2) and 6500 m (samplesBA1).

Stage D: Chattian-early Miocene (ending at ~20 Ma). The Chattian-early Miocene stage corresponds to the Fiscal and Guarga thrusting, responsible for most of the displacement on the frontal ramp in the Sierras Exteriores. The Campodarbe sedimentation is interrupted in the Jaca Basin by the uplift related to the Fiscal thrusting onset, while it continues during the early-middle Chattian in the Ebro Basin, where it is followed by the Uncastillo Formation. The frontal ramp propagates with a system of break-back thrusting at the leading edge associated with deposition of the Uncastillo conglomerate. The end of this stage also marks the end of the south Pyrenean compression observable in the geological record. Uplift related to the Fiscal-Guarga thrusting is responsible for most of the exhumation of the Hecho Group turbidites (TUR 3 is the deepest sample at 3.3 km at the end of the stage) and Axial Zone basement (with samples GV2 and BA1 at 3 km and 1.5 km, respectively). Assuming a mean geothermal gradient of 30°C/km, these burial depths at ~20 Ma accord with the main single-grain age population of samples GV2, JA2, and JA3 (25.6, 26.8, and 23.3 Ma, respectively), assumed to have been totally reset. Samples BA8 and GV5 located deeper in the Axial Zone were exhumed around the end of the stage (central ages of 20.5 ± 1.8 and 18.2 ± 1.2 Ma, respectively). On the other hand, the 6.5 km burial depth of BA1 at 29 Ma appears too deep compared to its central age of 29.3 ± 2.7 Ma. However, *Bosch et al.* [2016] published zircon (U-Th)/He ages of 22.1 ± 1.2 Ma, 22 ± 14.7 Ma, and 23.7 ± 2.3 Ma for samples BA1, BA5, and BA8, respectively, and their QTQt modeling shows fast exhumation of these samples between 30 Ma and 20 Ma, consistent with our structural restoration. The central ages of the totally reset turbidite samples and the ages of the main single-grain populations in the partially reset ones (Figures 10b and 11) also attest to their exhumation during the Fiscal-Guarga thrusting stage.

Stage E. The situation after erosion and isostatic uplift of the belt. During all stages, the samples located south of the Oturia thrust remain at burial depths not exceeding 3 km, consistently with their low reset level. In these samples, the numerous Late Cretaceous to Paleogene single-grain ages probably refer to the exhumation of the sources during the earliest stages of the Pyrenean orogeny.

5.1. Geothermal Gradients

The maximum burial depths attained at stage C by the basin fill allow estimating geothermal gradients and clarifying the distribution of the temperature anomalies deduced from thermometry data (cf. sections 4.2.3 and 4.4; Figure 8 and Table 2). In the western part of the study area, most of the turbidite samples (TUR3, BC2, CT2, BC1, OT7, and OT3) yield vitrinite and Raman-derived temperatures corresponding to rather low geothermal gradients between 23 and 26°C/km, coherent with the foreland basin context. By contrast, samples OT4 and OT5 correspond to higher gradients (35–36°C/km), which supports the temperature anomaly already inferred along the Oturia thrust fault. In the northeastern area, the maximum temperatures in the turbidites also correspond to higher gradients: 29–31°C/km for samples OR19 and CT1, respectively, and 33°C/km (Raman) or 38°C/km (vitrinite) for sample OR16. However, if we retain the temperature of 170°C given for the latter sample by the QTQt modeling, we obtain a gradient of 31°C/km equivalent to those calculated for OR19 and CT1. Calculated gradients are much higher for samples at the base of the turbidite

succession in the Ordesa area (36°C/km and 44°C/km for samples OR14 and OR20, respectively, when projecting these samples according to their actual altitude, i.e., 1000 m lower than shown in Figure 14; see comment on this point in section 4.1.3). These results confirm the temperature anomaly already inferred from the high gradient between samples OR16–OR19 and the Ordesa samples, and from the QTQt modeling. The calculated 31°C/km gradient, higher than in the western area, may be an artifact related to a deeper burial in the north-east than that inferred on our restoration. However, owing to the thermal anomaly confirmed for the lowermost turbidites in that area, we think more likely that the gradient around 25°C/km calculated in western area corresponds to the burial gradient and that the higher gradient in the northeastern area traduces the thermal anomaly in the medium part of the turbidite succession. As discussed above, the thermal anomalies may have occurred during stage A (and B?) in the northeast and stage B along the Oturia thrust. We note that a regional gradient of 25°C/km at stage C in the northern part of the Jaca Basin is consistent with the present-day mean gradient of 22.6°C/km in the detached South Pyrenean Unit [*Fernández et al.*, 1998].

5.2. Comparison With the Axial Zone North of the Ainsa Basin

Our restoration shows that the Axial Zone, corresponding to the top of the Gavarnie culmination, was exhumed more recently than in the transect located 30 km to the east studied by *Jolivet et al.* [2007], where a sample from the Néouvielle summit (NV1 in Figure 2) yielded an AFT central age of 35.1 ± 2.3 Ma in spite of being at a similar altitude and equivalent structural position than BA1. By contrast, sample GV5 at the Gavarnie thrust footwall yielded an AFT central age of 18.2 ± 1.2 Ma similar to the 18–19 Ma central ages obtained 15 km eastward at the top of the Bielsa granite in an equivalent structural position (samples BS1 and BS7 in Figure 2) [*Jolivet et al.*, 2007]. The latter samples are located at different altitudes along the southward tilted top surface of the Bielsa granite while sample BS6, which was collected in the core of the massif at higher altitude than BS7, yielded a much younger age of 10.9 ± 1.0 Ma. These results lead *Jolivet et al.* [2007] to propose that tilting of the top of the basement was a Miocene event related to out-of-sequence thrusting on the Bielsa thrust. On the cross section studied here, the Broto thrust, equivalent to the Bielsa thrust, does not show evidence of out-of-sequence thrusting. It is, however, possible that the late tilting of the Bielsa granite corresponded to a late tightening of the Bielsa antiformal culmination not related to large displacement on the thrust itself and without equivalent in the studied section. The Néouvielle-Bielsa section thus shows both an earlier onset and a later end of exhumation of the central and southern Axial Zone when compared to the cross section presented here. These differences are consistent with the fact that the two sections belong to different segments of the Axial Zone, separated by a zone of westward plunge of the structure.

6. Conclusions

The combination of surface data and interpreted seismic profiles of the eastern Jaca thrust-sheet-top basin of the southern Pyrenees is used to refine its deep structure and leads to the definition of new thrusts in the basement (the Broto and Fiscal thrusts) and in the lowermost foreland basin sequences (the Oturia and Yebra de Basa thrusts across the Upper Cretaceous-Eocene carbonates). New constraints for unraveling the kinematic relationships between basement and cover structures are provided. We define a piggyback basement thrusting sequence involving, from north to south, the Eaux-Chaudes, Gavarnie, Broto, Fiscal, and Guarga thrusts from the early Eocene to the early Miocene. The four latter thrusts cumulated a total shortening of about 36 km, with shortening rates decreasing from 2.2 mm/yr (Gavarnie-Broto) to 1.7 mm/yr (Fiscal-Guarga). In particular, we confirm the Priabonian (-early Rupelian) age of the Gavarnie thrust proposed in previous studies [*Mutti et al.*, 1988; *Teixell*, 1996]. Shortening on the Eaux-Chaudes thrust, in the hinterland of the Jaca Basin, remains undetermined but at least about 5 km were transferred to the northern part of the Jaca Basin during the Lutetian-Bartonian in the Monte Perdido thrust sheet. Hence, a total of about 41 km of shortening is recorded along this transverse of the Jaca Basin, corresponding to 47% of the restored original length.

The Jaca Basin experienced large vertical movements due to basement-involved thrusting, with up to 9 km structural relief, which allowed for the deposition of a thick synorogenic sedimentary sequence. This is highlighted by increasing levels of resetting of apatite fission tracks going northward and downward in the foreland basin sequence, with samples in the lower Hecho Group turbidites completely reset at temperatures around 170–180°C. The correlation between reset level and stratigraphic position shows that burial of the synorogenic sediments was mainly due to the sedimentary accumulation rather than burial below thrust units. Sequential structural restoration and distribution of maximum paleotemperatures derived from

measurements of organic matter maturation show that maximal burial was reached during the Broto thrusting stage (Rupelian) with a moderate geothermal gradient around 25°C/km characteristic of such a foreland setting. However, thermometry in the northeastern part of the study area reveals maximum paleotemperatures up to 240°C at the base of the turbidite succession. The distribution of these high temperatures and the high gradient they imply in the lower part of the succession (around 50°C/km in the first kilometer) argue for transient anomalies due to fluid circulation during emplacement of the Monte Perdido and Gavarnie thrust systems. Fluid circulation during the younger Gavarnie thrusting stage also explains unexpectedly high temperatures found around the Oturia thrust.

The central ages of completely reset fission track samples in the Axial Zone and northern Jaca Basin and the main statistical single-grain age populations in the partially reset turbidite samples show that the main exhumation across the Partial Annealing Zone occurred during the late Oligocene-early Miocene, in relation to hanging wall uplift of the Fiscal and Guarga thrusts. These results show that exhumation of the middle part of the Axial Zone (Gavarnie thrust sheet) is younger than further east where previous studies showed it to be Priabonian in age [*Jolivet et al.*, 2007]. Furthermore, we found no structural evidence for early Miocene out-of-sequence reactivation of the Broto thrust, as earlier deduced from fission track data for the equivalent Bielsa thrust east of the study area [*Jolivet et al.*, 2007].

This study demonstrates that the understanding of the tectonothermal evolution of a foreland basin needs to take into account a variety of controlling factors as the history of deformation propagation into the basin, the pattern of transient hot fluid circulation in the fault and fracture system, and the specific time scales of the different processes that left signature in the paleothermometric and thermochronologic record. In particular, we show that the maximum paleotemperatures derived from organic matter maturation may not be usable for deriving paleogeothermal gradients related to the burial history, while apatite fission track analysis may be more appropriate.

Appendix A: Thermometry and Thermochronology Methodology

Vitrinite reflectance measurement methodology: Vitrinite analyses were realized at the Centre Scientifique et Technique Jean-Féger, Total, Pau, France. Due to their low concentration in vitrinite, the samples were ground and densimetric concentrates of organic matter were obtained by flotation in heavy liquids. Concentrates were mounted in epoxy resin and polished. Mean reflectance measurements were realized in oil immersion at 500X magnification under incident nonpolarized white light. Qualitative observation of fluorescence colors was used for identification of organic matter types and for confirming the maturity rank. For each sample, the result given is the mean value of, as far as possible, at least 30 measurements.

Raman spectroscopy methodology: The instrument used in this study is a Renishaw InVIA Reflex microspectrometer of the Ecole Normale Supérieure, Paris, France, coupled to a DMLM Leica microscope equipped with four objectives of 5X, 20X, 50X, and 100X magnification. The excitation laser was an argon laser ($\lambda 0 = 514.5$ nm, source power 20 mW but only about 1 mW reach the sample surface) focused on carbonaceous material using an 100X objective (NA = 0.90). The instrument control and Raman measurements were operated with the software packages Renishaw Wire. Raman measurements were carried out on polished thin sections prepared following the analysis protocol described in *Beyssac et al.* [2002] and *Lahfid et al.* [2010]. These samples being likely to contain detrital CM, their internal structural heterogeneity has been checked by measuring 10–15 spectra for each sample.

Apatite fission track methodology: The apatite grains were mounted on glass slides using epoxy glue and polished. Samples were etched in 6.5% HNO3 for 45 s at 20°C to reveal the spontaneous fission tracks, before being irradiated with a neutron flux of 1.0×10^{16} neutrons cm^{-2} (Oregon State University). The external detector method [*Hurford*, 1990a, 1990b] was used for the age determination with micas as external detectors. These were etched in 40% HF for 40 min at 20°C to reveal the induced tracks. The ages were calculated following the method recommended by the Fission Track Working Group of the IUGS Subcommission on Geochronology [*Hurford*, 1990a and b] using the zeta calibration method [*Hurford and Green*, 1983] and the Trackkey software (Dunkl, University of Tuebingen). CN5 glass was used as dosimeter with a zeta factor of 342.66 ± 6.67 (F. Meresse), obtained on both Durango and Mount Dromedary apatite standards. Fission tracks were counted on a Zeiss Axioplan microscope, using a magnification of 1250 under dry objectives.

References

Arehart, G. B., and R. A. Donelick (2006), Thermal and isotopic profiling of the Pipeline hydrothermal system: Application to exploration for Carlin-type gold deposits, *J. Geochem. Explor.*, *91*, 27–40.

Arenas, C. (1993), Sedimentología y paleogeografía del Terciario del margen pirenaico y sector central de la Cuenca del Ebro (zona aragonesa occidental), PhD thesis, Univ. de Zaragoza, Zaragoza, Spain.

Arenas, C., H. Millán, G. Pardo, and A. Pocovi (2001), Ebro basin continental sedimentation associated with late compressional Pyrenean tectonics (northeastern Iberia): Controls on basin margin fans and fluvial systems, *Basin Res.*, *13*, 65–89.

Babault, J., J. Van Den Driessche, and S. Bonnet (2005), Origin of the highly elevated Pyrenean peneplain, *Tectonics*, *24*, TC2010, doi:10.1029/2004TC001697.

Barbarand, J., A. Carter, I. Wood, and T. Hurford (2003a), Compositional and structural control of fission-track annealing in apatite, *Chem. Geol.*, *198*, 107–137.

Barbarand, J., A. Carter, and T. Hurford (2003b), Variation in apatite fission-track length measurement: Implications for thermal history modelling, *Chem. Geol.*, *198*, 77–106.

Barker, C. E., and M. J. Pawlewicz (1994), Calculation of vitrinite reflectance from thermal history and peak temperatures. A comparison of methods, in *Reevaluation of Vitrinite Reflectance*, *Am. Chem. Soc. Symp. Ser.*, vol. 570, edited by P. K. Mukhopadhyay and W. G. Dow, pp. 216–229, Am. Chem. Soc., Washington, D. C.

Barnolas, A., and A. Teixell (1994), Platform sedimentation and collapse in a carbonate dominated margin of a foreland basin (Jaca basin, Eocene, southern Pyrenees), *Geology*, *22*, 1107–1110.

Barnolas, A., and J.-C. Chiron (Eds) (1996), *Synthèse Géologique et Géophysique des Pyrénées. Volume 1: Introduction, Géophysique, Cycle Hercynien*, Bureau de Recherches Géologiques et Minières, Orléans, France & Instituto Tecnologico Geominero de España, Madrid, Spain.

Beamud, E., J. A. Muñoz, P. G. Fitzgerald, S. Baldwin, M. Garcés, L. Cabrera, and J. R. Metcalf (2010), Magnetostratigraphy and detrital apatite fission track thermochronology in syntectonic conglomerates: Constraints on the exhumation of the South-Central Pyrenees, *Basin Res.*, doi:10.1111/j.1365-2117.2010.00492.x.

Beaumont, C., J. A. Muñoz, J. Hamilton, and P. Fullsack (2000), Factors controlling the Alpine evolution of the central Pyrenees inferred from a comparison of observations and geodynamical models, *J. Geophys. Res.*, *105*, 8121–8145, doi:10.1029/1999JB900390.

Beyssac, O., B. Goffe, C. Chopin, and J.-N. Rouzaud (2002), Raman spectra of carbonaceous material in metasediments: A new geothermometer, *J. Metamorph. Geol.*, *20*, 859–871.

Bosch, G., A. Teixell, M. Jolivet, P. Labaume, D. Stockli, M. Domènech, and P. Monié (2016), Record of Eocene-Miocene thrusting in the western Axial Zone and Chaînons Béarnais (west-central Pyrenees) revealed by multi-method thermochronology, *C. R. Geosci.*, doi:10.1016/j.crte.2016.01.001.

Brandon, M. T. (2002), Decomposition of mixed age distributions using Binomfit, *Track*, *24*, 13–18.

Braun, J., P. Van der Beek, and G. Batt (2006), *Quantitative Thermochronology; Numerical Methods for the Interpretation of Thermochronological Data*, Cambridge Univ. Press, New York.

Burtner, R., A. Nigrini, and R. A. Donelick (1994), Thermochronology of lower Cretaceous source rocks in the Idaho-Wyoming Thrust belt, *Am. Assoc. Petrol. Geol. Bull.*, *78*, 1613–36.

Caja, M. A., R. Marfil, D. Garcia, E. Remacha, S. Morad, H. Mansurbeg, A. Amorosi, C. Martinez-Calvo, and R. Lahoz-Beltra (2009), Provenance of siliciclastic and hybrid turbiditic arenites of the Eocene Hecho Group, Spanish Pyrenees: Implications for the tectonic evolution of a foreland basin, *Basin Res.*, doi:10.1111/j.1365-2117.2009.00405.x.

Cámara, P., and J. Klimowitz (1985), Interpretación geodinámica de la vertiente centro-occidental surpirenaica, *Estud. Geol.*, *41*, 391–404.

Carlson, W. D., R. A. Donelick, and R. A. Ketcham (1999), Variability of apatite fission-track annealing kinetics: I. Experimental results, *Am. Mineral.*, *8*, 1213–1223.

Casas, A. M., B. Oliva, T. Roman-Berdiel, and E. Pueyo (2003), Basement deformation: Tertiary folding and fracturing of the Variscan Bielsa granite (Axial Zone, central Pyrenees), *Geodyn. Acta*, *16*, 99–117.

Cohen, K. M., S. C. Finney, P. L. Gibbard, and J.-X. Fan (2013), The ICS International Chronostratigraphic Chart, *Episodes*, *36*, 199–204. [Available at http://www.stratigraphy.org/ICSchart/ChronostratChart2014-10.pdf.]

Coney, P. J., J. A. Muñoz, K. R. McClay, and C. A. Evenchick (1996), Syntectonic burial and post-tectonic exhumation of the southern Pyrenees foreland fold-thrust belt, *J. Geol. Soc., London*, *153*, 9–16.

Crowley, K. D., M. Cameron, and R. L. Schaefer (1991), Experimental studies of annealing of etched fission tracks in fluorapatite, *Geochim. Cosmochim. Acta*, *55*, 1449–1465.

Dahlen, F. A. (1990), Critical taper model of fold-and-thrust belts and accretionary wedges, *Annu. Rev. Earth Planet. Sci.*, *18*, 55–99.

Das Gupta, K., and K. T. Pickering (2008), Petrography and temporal changes in petrofacies of deep-marine Ainsa-Jaca basin sandstone systems, early and middle Eocene, Spanish Pyrenees, *Sedimentology*, *55*, 1083–1114.

Davis, D., J. Suppe, and F. A. Dahlen (1983), Mechanics of fold-and-thrust belts and accretionary wedges, *J. Geophys. Res.*, *88*(B2), 1153–72, doi:10.1029/JB088iB02p01153.

Dengfa, H., and J. Suppe (Eds.) (2005), Guidebook for field trip in south and north Tianshan foreland basin, Xinjiang Uygur Autonomous Region, China, International Conference on Theory and Application of Fault-related Folding in Foreland Basins, PetroChina, Beijing, China.

Donelick, R. A. (1993), A method of fission track analysis utilizing bulk chemical etching of apatite, Patent 5267274.

Donelick, R. A. (1995), A method of fission track analysis utilizing bulk chemical etching of apatite, Patent 658800, Aust.

Donelick, R. A., P. B. O'Sullivan, and R. A. Ketcham (2005), Apatite fission-track analysis, in *Low-Temperature Thermochronology: Techniques, Interpretations and Applications*, vol. 58, edited by P. W. Reiners, pp. 49–94, Mineralog. Soc. of Am. and Geochem. Soc., Washington, D. C.

Dreyer, T., J. Corregidor, P. Arbues, and C. Puigdefàbregas (1999), Architecture of the tectonically influenced Sobrabe deltaic complex in the Ainsa Basin, northern Spain, *Sediment. Geol.*, *127*, 127–169.

Fernández, M., I. Marzan, A. Correia, and E. C. Ramalho (1998), Heat flow, heat production, and lithospheric thermal regime in the Iberian Peninsula, *Tectonophysics*, *291*, 29–53.

Fernández, O., J. A. Muñoz, P. Arbués, and O. Falivene (2012), 3D structure and evolution of an oblique system of relaying folds: The Ainsa basin (Spanish Pyrenees), *J. Geol. Soc., London*, *169*, 545–559, doi:10.1144/0016-76492011-068.

Filleaudeau, P.-Y., F. Mouthereau, and R. Pik (2012), Thermo-tectonic evolution of the south-central Pyrenees from rifting to orogeny: Insights from detrital zircon U/Pb and (U Th)/He thermochronology, *Basin Res.*, *24*, 401–417.

Fillon, C., C. Gautheron, and P. Van Der Beek (2013), Oligocene–Miocene burial and exhumation of the Southern Pyrenean foreland quantified by low-temperature thermochronology, *J. Geol. Soc., London*, *170*, 67–77.

Fitzgerald, P. G., R. B. Sorkhabi, T. F. Redfield, and E. Stump (1995), Uplift and denudation of the central Alaska Range: A case study in the use of apatite fission track thermochronology to determine absolute uplift parameters, *J. Geophys. Res.*, *100*, 20,175–20,191, doi:10.1029/95JB02150.

Fitzgerald, P. G., J. A. Muñoz, P. J. Coney, and S. L. Baldwin (1999), Asymmetric exhumation across the Pyrenean orogen: Implication for the tectonic evolution of a collisional orogen, *Earth Planet. Sci. Lett.*, *173*, 157–170.

Galbraith, R. F. (1990), The radial plot: Graphical assessment of spread in ages, *Nucl. Tracks Radiat. Meas.*, *17*, 207–214.

Galbraith, R. F. (2005), *Statistics for Fission Track Analysis*, Chapman & Hall/CRC, Boca Raton, Fla.

Galbraith, R. F., and G. M. Laslett (1993), Statistical models for mixed fission track ages, *Nucl. Tracks Radiat. Meas.*, *21*, 459–470.

Galbraith, R. F., and P. F. Green (1990), Estimating the component ages in a finite mixture, *Nucl. Tracks Radiat. Meas.*, *17*, 197–206.

Gallagher, K. (2012), Transdimensional inverse thermal history modelling for quantitative thermochronology, *J. Geophys. Res.*, *117*, B02408, doi:10.1029/2011JB00882.

Gallagher, K., R. Brown, and C. Johnson (1998), Fission track analysis and its applications to geological problems, *Annu. Rev. Earth Planet. Sci.*, *26*, 519–572.

Galushkin, Y. I. (1997), Thermal effects of igneous intrusions on maturity of organic matter: A possible mechanism of intrusion, *Org. Geochem.*, *26*, 645–658.

Gibson, M., H. D. Sinclair, G. J. Lynn, and F. M. Stuart (2007), Late- to post-orogenic exhumation of the Central Pyrenees revealed through combined thermochronological data and modeling, *Basin Res.*, *19*, 323–334.

Gil Peña, I., M. J. Montes Santiago, and J. Malago Luesma (1990), Biescas, Mapa Geológico de España scale 1:50,000, sheet 177, Instituto Geólogico y Minero de España, Madrid, Spain.

Gradstein, F. M., et al. (2012), *The Geologic Time Scale 2012*, Elsevier, Boston, doi:10.1016/B978-0-444-59425-9.00004-4.

Green, P. F., I. R. Duddy, A. J. W. Gleadow, P. R. Tingate, and G. M. Laslett (1985), Fission track annealing in apatite: Track length measurements and the form of the Arrhenius plot, *Nucl. Tracks Radiat. Meas.*, *10*, 323–328.

Harrison, J. C. (1995), Melville Island's salt-based fold belt, Arctic Canada Geol. Surv. of Can., Bull., 472, 331 pp.

Hogan, P. J., and K. D. W. Burbank (1996), Evolution of the Jaca piggy-back basin and emergence of the External Sierras, southern Pyrenees, in *Tertiary Basins of Spain*, edited by P. F. Friend and C. J. Dabrio, pp. 153–160, Cambridge Univ. Press, Cambridge, U. K.

Holl, J. E., and D. J. Anastasio (1995), Cleavage development within a foreland fold and thrust belt, southern Pyrenees, Spain, *J. Struct. Geol.*, *17*, 357–369.

Huang, W.-L. (1996), Experimental study of vitrinite maturation: Effects of temperature, time, pressure, water, and hydrogen index, *Org. Geochem.*, *24*, 233–241.

Hurford, A. J. (1990a), International Union of Geological Sciences Subcommission on Geochronology recommendation for the standardization of fission track dating calibration and data reporting, *Nucl. Tracks Radiat. Meas.*, *17*, 233–36.

Hurford, A. J. (1990b), Standardization of fission track dating calibration: Recommendation by the Fission Track Working Group of the I.U.G.S. Subcommission on Geochronology, *Chem. Geol.*, *80*, 171–78.

Hurford, A. J., and P. F. Green (1983), The zeta age calibration of fission-track dating, *Chem. Geol.*, *1*, 285–317.

Huygue, D., F. Mouthereau, S. Castelltort, P. Y. Filleaudeau, and L. Emmanuel (2009), Paleogene propagation of the southern Pyrenean thrust wedge revealed by finite strain analysis in frontal thrust sheets: Implications for mountain building, *Earth Panet. Sci. Lett.*, *288*, 421–433.

Instituto Geologico y Minero de España (1987), *Contribución de la Exploracion Petrolífera al Conocimiento de la Geología de España*, Instituto Geológico y Minero de España, Madrid, Spain.

Izquierdo-Llavall, E., L. Aldega, V. Cantarelli, S. Corrado, I. Gil-Peña, C. Invernizzi, and A. M. Casas (2013), On the origin of cleavage in the Central Pyrenees: Structural and paleo-thermal study, *Tectonophysics*, *608*, 303–318, doi:10.1016/j.tecto.2013.09.027.

Jammes, S., G. Manatschal, L. Lavier, and E. Masini (2009), Tectonosedimentary evolution related to extreme crustal thinning ahead of a propagating ocean: Example of the western Pyrenees, *Tectonics*, *28*, TC4012, doi:10.1029/2008TC002406.

Jolivet, M., P. Labaume, P. Monié, M. Brunel, N. Arnaud, and M. Campani (2007), Thermochronology constraints for the propagation sequence of the south-Pyrenean basement thrust system (France-Spain), *Tectonics*, *26*, TC5007, doi:10.1029/2006TC002080.

Labaume, P., E. Mutti, M. Séguret, and J. Rosell (1983), Mégaturbidites carbonatées du bassin turbiditique de l'Eocène inférieur et moyen sud-pyrénéen, *Bull. Soc. Geol. Fr.*, *25*, 927–941.

Labaume, P., M. Séguret, and C. Seyve (1985), Evolution of a turbiditic foreland basin and analogy with an accretionary prism: Example of the Eocene South-Pyrenean Basin, *Tectonics*, *4*, 661–685, doi:10.1029/TC004i007p00661.

Labaume, P., E. Mutti, and M. Séguret (1987), Megaturbidites: A depositional model from the Eocene of the SW-Pyrenean Foreland Basin, Spain, *Geo Mar. Lett.*, *7*, 91–101.

Lacroix, B., M. Buatier, P. Labaume, A. Travé, M. Dubois, D. Charpentier, S. Ventalon, and D. Convert-Gaubier (2011), Microtectonic and geochemical characterization of thrusting in a foreland basin: Example of the South-Pyrenean orogenic wedge (Spain), *J. Struct. Geol.*, *33*, 1359–1377.

Lacroix, B., D. Charpentier, M. Buatier, T. Vennemann, P. Labaume, T. Adatte, A. Travé, and Dubois (2012), Formation of chlorite during thrust fault reactivation. Record of fluid origin and P–T conditions in the Monte Perdido thrust fault (southern Pyrenees), *Contrib. Mineral. Petrol.*, *163*(6), 1083–1102, doi:10.1007/s00410-011-0718-0.

Lacroix, B., A. Travé, M. Buatier, P. Labaume, T. Vennemann, and M. Dubois (2014), Syntectonic fluid-flow along thrust faults: Example of the South-Pyrenean fold-and-thrust belt, *Mar. Pet. Geol.*, *49*, 84–98, doi:10.1016/j.marpetgeo.2013.09.005.

Lagabrielle, Y., P. Labaume, and M. de Saint-Blanquat (2010), Mantle exhumation, crustal denudation and gravity tectonics during Cretaceous rifting in the Pyrenean realm (SW Europe): Insights from the geological setting of the lherzolite bodies, *Tectonics*, *29*, TC4012, doi:10.1029/2009TC002588.

Lahfid, A., O. Beyssac, E. Deville, F. Negro, and B. Goffé (2010), Evolution of the Raman spectrum of carbonaceous material in low-grade metasediments of the Glarus Alps (Switzerland), *Terra Nova*, *22*, 354–360.

Le Bayon, R., S. Buhre, B. C. Schmidt, and R. Ferreiro Mählmann (2012), Experimental organic matter maturation at 2 kbar: Heat-up effect to low temperatures on vitrinite reflectance, *Int. J. Coal Geol.*, *92*, 45–53.

Maurel, O., P. Monié, R. Pik, A. Arnaud, M. Brunel, and M. Jolivet (2008), The Meso-Cenozoic thermo-tectonic evolution of the Eastern Pyrenees: An Ar-40/Ar-39 fission track and (U-Th)/He thermochronological study of the Canigou and Mont-Louis massifs, *Int. J. Earth Sci.*, *97*, 565–584.

McCulloch, A. A. (1994), Low temperature thermal history of eastern Ireland: Effects of fluid flow, *Mar. Pet. Geol.*, *11*, 389–399.

Metcalf, J. R., P. G. Fitzgerald, S. L. Baldwin, and J. A. Muñoz (2009), Thermochronology of a convergent orogen: Constraints on the timing of thrust faulting and subsequent exhumation of the Maladeta pluton in the Central Pyrenean Axial Zone, *Earth Planet. Sci. Lett.*, *287*, 488–503.

Millán Garrido, H. (2006), Estructura y cinemática del frente de cabalgamiento surpirenaico en las Sierras Exteriores aragonesas, in *Colección de Estudios Altoaragoneses*, vol. 53, Instituto de Estudios Altoaragoneses, Huesca, Spain.

Millán Garrido, H., E. L. Pueyo Morer, M. Aurell Cardona, A. Aguado Luzón, B. Oliva Urcia, M. B. Martínez Peña, and A. Pocoví (2000), Actividad tectonica registrada en los depósitos terciarios del frente meridional del Pirineo central, *Rev. Soc. Geol. Esp.*, *13*, 279–300.

Millán Garrido, H., B. Oliva Urcia, and A. Pocoví Juan (2006), La transversal de Gavarnie-Guara. Estructura y edad de los mantos de Gavarnie, Guara-Gèdre y Guarga (Pirineo centro-occidental), *Geogaceta*, *40*, 35–38.

Mochales, T., A. M. Casas, E. L. Pueyo, and A. Barnolas (2012), Rotational velocity for oblique structures (Boltaña anticline, Southern Pyrenees), *J. Struct. Geol.*, *35*, 2–16, doi:10.1016/j.jsg.2011.11.009.

Montes Santiago, M. J. (1991), Yebra de Basa, Mapa Geológico de España scale 1:50,000, sheet 210, Instituto Geológico y Minero de España, Madrid, Spain.

Montes Santiago, M. J. (1992), Sistemas depositionales en el Eoceno medio-Oligoceno del sinclinorio del Guarga (Cuenca de Jaca, Pirineo central), in *Simposio sobre Geología de los Pirineos*, *III Congreso Geológico de España*, vol. 2, pp. 150–160, Sociedad Geológica de España, Salamanca, España.

Morris, R. G., H. D. Sinclair, and A. J. Yelland (1998), Exhumation of the Pyrenean orogen: Implications for sediment discharge, *Basin Res.*, *10*, 69–85.

Mouthereau, F., P.-Y. Filleaudeau, A. Vacherat, A. Pik, A. O. Lacombe, M. G. Fellin, S. Castelltort, F. Christophoul, and E. Masini (2014), Placing limits to shortening evolution in the Pyrenees: Role of margin architecture and implications for the Iberia/Europe convergence, *Tectonics*, *33*, 2283–2314, doi:10.1002/2014TC003663.

Muñoz, J. A. (1992), Evolution of a continental collision belt: ECORS-Pyrenees crustal balanced cross-section, in *Thrust Tectonics*, edited by K. R. McClay, pp. 235–246, Chapman & Hall, London, U. K.

Muñoz, J. A., E. Beamud, O. Fernández, P. Arbués, J. Dinarès-Turell, and J. Poblet (2013), The Ainsa fold and thrust oblique zone of the central Pyrenees: Kinematics of a curved contractional system from paleomagnetic and structural data, *Tectonics*, *32*, 1142–1175, doi:10.1002/tect.20070.

Mutti, E., M. Séguret, and M. Sgavetti (1988), Sedimentation and deformation in the Tertiary sequences of the Southern Pyrenees. Field Trip 7 guidebook AAPG Mediterranean Basins Conference, Nice, France, Special Publication of the Institute of Geology of the Univ. of Parma, Parma, Italy.

O'Brien, G. W., M. Lisk, I. R. Duddy, J. Hamilton, P. Woods, and R. Cowley (1999), Plate convergence, foreland development and fault reactivation: Primary controls on brine migration, thermal histories and trap breach in the Timor Sea, Australia, *Mar. Pet. Geol.*, *16*, 533–560.

Oliva-Urcia, B., E. Beamud, M. Garcés, C. Arenas, R. Soto, E. L. Pueyo, and G. Pardo (2015), New magnetostratigraphic dating in the Palaeogene syntectonic sediments of the west-central Pyrenees: Tectonostratigraphic implications, in *Palaeomagnetism in Fold and Thrust Belts: New Perpectives*, edited by E. L. Pueyo, *Geol. Soc. Spec. Publ.*, 425, doi:10.1144/SP425.5.

Oms, O., J. Dinarès-Turell, and E. Remacha (2003), Magnetic stratigraphy from deep clastic turbidites: An example from the Eocene Hecho Group (southern Pyrenees), *Stud. Geophys. Geod.*, *47*, 275–288.

Payros, A., V. Pujalte, and X. Orue-Etxebarria (1999), The South-Pyrenean Eocene carbonate megabreccias revisited: New interpretation based on evidence from the Pamplona Basin, *Sediment. Geol.*, *125*, 165–194.

Poblet, J., and S. Hardy (1995), Reverse modeling of detachment folds—Application to the Pico-del-Aguila anticline in the South-Central Pyrenees (Spain), *J. Struct. Geol.*, *17*, 1707–1724.

Pueyo, E. L., H. Millán, and A. Pocovı (2002), Rotation velocity of a thrust: A paleomagnetic study in the External Sierras (Southern Pyrenees), *Sediment. Geol.*, *146*, 191–208.

Puigdefàbregas, C., and P. Souquet (1986), Tecto-sedimentary cycles and depositional sequences of the Mesozoic and Tertiary from the Pyrenees, *Tectonophysics*, *129*, 173–203.

Puigdefábregas Tomás, C. (1975), La sedimentation molásica en la cuenca de Jaca, *Pirineos*, *104*, 1–188.

Rahl, J. M., S. H. Haines, and B. A. van der Pluijm (2011), Links between orogenic wedge deformation and erosional exhumation: Evidence from illite age analysis of fault rock and detrital thermochronology of syn-tectonic conglomerates in the Spanish Pyrenees, *Earth Planet. Sci. Lett.*, *307*, 180–190, doi:10.1016/j.epsl.2011.04.036.

Remacha, E., P. Arbués, and M. Carreras (1987), Precisiones sobre los limites de la secuencia deposicional de Jaca. Evolución de las facies desde la base de la secuencia hasta el techo de la arenisca de Sabiñánigo, *Bol. Geol. Min.*, *98*, 40–48.

Remacha, E., L. P. Fernández, E. Maestro, O. Oms, R. Estrada, and A. Teixell (1998), The Upper Hecho Group turbidites and their vertical evolution to deltas (Eocene, South-Central Pyrenees), International Association of Sedimentologists, 15th International Sedimentological Congress, Alicante, Field Trip Guidebook, 1-25.

Remacha, E., G. Gual, F. Bolaño, M. Arcuri, O. Oms, F. Climent, P. Crumeyrolle, L. P. Fernandez, J. C. Vicente, and J. Suarez (2003), *Sand-rich Turbidite Systems of the Hecho Group From Slope to the Basin Plain. Facies, Stacking Patterns, Controlling Factors and Diagnostic Features*, *Geol. Field Trip*, no. 12, South-Central Pyrenees, AAPG International Conference and Exhibition, Barcelona, Spain.

Rios Aragües, L. M., J. M. Galera Fernández, and D. Barettino Fraile (1990), Sallent, Mapa Geologico de España scale 1:50,000, sheet 145, Instituto Geologico y Minero de España, Madrid, Spain.

Roigé, M., D. Gomez-Gras, E. Remacha, R. Daza, and S. Boya (2016), Tectonic control on sediment sources in the Jaca basin (middle and upper Eocene of the South-Central Pyrenees), *C. R. Geosci.*, doi:10.1016/j.crte.2015.10.005.

Roure, F., P. Choukroune, X. Berastegui, J. A. Munoz, A. Villien, P. Matheron, M. Bareyt, M. Séguret, P. Cámara, and J. Deramond (1989), ECORS deep seismic data and balanced cross-sections—Geometric constraints on the evolution of the Pyrenees, *Tectonics*, *8*, 41–50, doi:10.1029/TC008i001p00041.

Rushlow, C. R., J. B. Barnes, T. A. Ehlers, and J. Vergés (2013), Exhumation of the southern Pyrenean fold-thrust belt (Spain) from orogenic growth to decay, *Tectonics*, *32*, 843–860, doi:10.1002/tect.20030.

Sadezky, A., H. Muckenhuber, H. Grothe, R. Niessner, and U. Pöschl (2005), Raman microspectroscopy of soot and related carbonaceous materials: Spectral analysis and structural information, *Carbon*, *43*, 1731–1742.

Séguret, M. (1972), *Etude Tectonique des Nappes et Séries Décollées de la Partie Centrale du Versant sud des Pyrénées*, *Sér. Géol. Struct.*, vol. 2, Publications de l'Univ. des Sciences et Techniques du Languedoc, Montpellier, France.

Sinclair, H. D., M. Gibson, M. Naylor, and R. G. Morris (2005), Asymmetric growth of the Pyrenees revealed through measurement and modeling of orogenic fluxes, *Am. J. Sci.*, *305*, 369–406.

Sobel, E. R., and D. Seward (2010), Influence of etching conditions on apatite fission-track etch pit diameter, *Chem. Geol.*, *271*, 59–69.

Soler-Sampere, M., and C. Puigdefàbregas-Tomás (1970), Lineas generales de la geologia del Alto Aragón occidental, *Pirineos*, *96*, 5–20.

Suárez-Ruiz, I., D. Flores, J. G. Mendonça Filho, and P. C. Hackley (2012), Review and update of the application of organic petrology: Part 1, geological applications, *Int. J. Coal Geol.*, *99*, 54–112.

Suppe, J. (1983), Geometry and kinematics of fault-bend folding, *Am. J. Sci.*, *283*, 684–721.

Tagami, T. (2012), Thermochronological investigation of fault zones, *Tectonophysics*, *538-540*, 67–85.

Teixell, A. (1990), Alpine thrusts at the western termination of the Pyrenean Axial Zone, *Bull. Soc. Geol. Fr.*, *8*, 241–249.

Teixell, A. (1996), The Ansó transect of the southern Pyrenees: Basement and cover thrust geometries, *J. Geol. Soc.*, *153*, 301–310.

Teixell, A. (1998), Crustal structure and orogenic material budget in the west-central Pyrenees, *Tectonics*, *17*, 395–406, doi:10.1029/98TC00561.

Teixell, A., and J. Garcia-Sansegundo (1995), Estructura del sector central de la cuenca de Jaca (Pirineos meridionales). Structure of the central sector of the Jaca Basin, southern Pyrenees, *Rev. Soc. Geol. Esp.*, *8*, 215–228.

Teixell, A., P. Labaume, and Y. Lagabrielle (2016), The crustal evolution of the west-central Pyrenees revisited: Inferences from a new kinematic scenario, *C. R. Geosci.*, doi:10.1016/j.crte.2015.10.

Ten Haaf, E., R. Van Der Voo, and H. Wensink (1970), The S-External Pyrenees of Huesca, *Geol. Rundsch.*, *60*, 996–1009.

Ternet, Y., P. Barrère, J. Canérot, and C. Majesté-Menjoulas (2003), Laruns-Somport, Carte Géologique de la France sheet 1069, Bureau de Recherches Géologiques et Minières, Orléans, France.

Trincal, V., D. Charpentier, M. D. Buatier, B. Grobety, B. Lacroix, P. Labaume, and J.-P. Sizun (2014), Quantification of mass transfers and mineral transformations in a thrust fault (Monte Perdido thrust unit, southern Pyrenees, Spain), *Mar. Pet. Geol.*, *55*, 160–175, doi:10.1016/j.marpetgeo.2013.12.016.

Vacherat, A., F. Mouthereau, R. Pik, M. Bernet, C. Gautheron, E. Masini, L. LePourhiet, B. Tibari, and A. Lahfid (2014), Thermal imprint of rift-related processes in orogens as recorded in the Pyrenees, *Earth Planet. Sci. Lett.*, *408*, 296–306, doi:10.1016/j.epsl.2014.10.014.

Vergés, J., M. Fernández, and A. Martínez (2002), The Pyrenean orogen: Pre-, syn-, and post-collisional evolution, *J. Virtual Explorer*, *8*, 57–76.

Vermeesch, P. (2012), On the visualisation of detrital age distributions, *Chem. Geol.*, *312–313*, 190–194.

Wayne, D. M., and A. M. McCaig (1998), Dating fluid-flow in shear zones: Rb-Sr and U-Pb studies of syntectonic veins in the Néouvielle Massif, Pyrenees, in *Dating and Duration of Fluid Flow and Fluid-Rock Interactions*, edited by J. Parnell, *Geol. Soc. Spec. Publ.*, *144*, pp. 129–135.

Whitchurch, A. L., A. Carter, H. D. Sinclair, R. A. Duller, A. C. Whittaker, and P. A. Allen (2011), Sediment routing system evolution within a diachronously uplifting orogen: Insights from detrital zircon thermochronological analyses from the South-Central Pyrenees, *Am. J. Sci.*, *311*, 442–482, doi:10.2475/05.2011.03.

Wopenka, B., and J. D. Pasteris (1993), Structural characterization of kerogens to granulite-facies graphite: Applicability of Raman microprobe spectroscopy, *Am. Mineral.*, *78*, 533–557.

Yui, T. F., E. Huang, and J. Xu (1996), Raman spectrum of carbonaceous material: A possible metamorphic grade indicator for low-grade metamorphic rocks, *J. Metamorph. Geol.*, *14*, 115–124.